

See discussions, stats, and author profiles for this publication at: <https://www.researchgate.net/publication/368514370>

# Predicting range-dependent underwater sound propagation from structural sources in shallow water using coupled finite element/equivalent source computations

Article in Ocean Engineering · March 2023

DOI: 10.1016/j.oceaneng.2023.113904

---

CITATIONS

8

4 authors, including:



Tengjiao He  
Shanghai Jiao Tong University

18 PUBLICATIONS 60 CITATIONS

[SEE PROFILE](#)

---

READS

300



Erzheng Fang  
Harbin Engineering University

17 PUBLICATIONS 61 CITATIONS

[SEE PROFILE](#)

## Highlights

### **Predicting range-dependent underwater sound propagation from structural sources in shallow water using coupled finite element/equivalent source computations**

Tengjiao He,Bin Wang,Shiqi Mo,Erzheng Fang

- A coupled FE /ES computation scheme is proposed to predict the range-dependent underwater sound propagation from a structural source, providing benchmark-quality solutions and high numerical efficiency
- The proposed coupled FE /ES computation scheme can handle the coupling between the structural-acoustic radiation and horizontally inhomogeneous waveguides.
- A novel multilayer acoustic–elastic ESM is developed to extend the ESM-based acoustic propagation model, allowing sound speed inhomogeneities and range-dependent elastic seabeds to be accommodated
- The validity of an effective complex density fluid model is analyzed for calculating the waveguide field excited by a structural source.

Predicting range-dependent underwater sound propagation from structural sources in shallow water using coupled finite element/equivalent source computations

Tengjiao He<sup>a,1</sup>, Bin Wang<sup>a,\*1</sup>, Shiqi Mo<sup>b</sup> and Erzheng Fang<sup>b</sup>

<sup>a</sup>Key Laboratory of Marine Intelligent Equipment and System, Ministry of Education, Shanghai Jiao Tong University, Shanghai, 200240, P. R. China

<sup>b</sup>College of Underwater Acoustic Engineering, Harbin Engineering University, Harbin, 150001, P. R. China

---

## ARTICLE INFO

### Keywords:

range-dependent sound propagation  
structural acoustic radiation  
equivalent source method  
elastic seabed  
speed inhomogeneities

---

## ABSTRACT

Predictions of underwater sound propagation (USP) from structural sources in complex shallow-water environments are crucial for underwater navigation, communication, and localization. Modeling range-dependent USP in shallow water remains challenging because structural acoustic radiation is coupled with complex waveguide physics. This paper presents a coupled finite element (FE)/equivalent source (ES) computation scheme for predicting the range-dependent USP from a structural source. The scheme involves coupled vibroacoustic FE/ES analyses and waveguide-field ES computations. The former computes the structural vibration response and reproduces the structural-acoustic radiation at arbitrary spatial positions. The coupled vibroacoustic FE/ES analysis provides the input for the waveguide-field ES computations, which couple the structural-acoustic radiation with the shallow-water environment. A multilayer acoustic-elastic ES method (ESM) is developed to accommodate sound speed inhomogeneities and a range-dependent elastic seabed. Numerical simulations demonstrate the interactions of structural-acoustic radiation with two-dimensional topographies and internal solitary waves. The proposed scheme is extended to three dimensions by combining the coupled vibroacoustic FE/ES analysis with a pre-corrected fast Fourier transform-accelerated ESM. The results validate the proposed scheme and demonstrate its benchmark-quality solutions and high numerical efficiency, suggesting great application potential for optimizing the sonar performance at the preliminary design stage.

---

## 1. Introduction

Control of underwater radiated noise (URN) from structural sources, such as surface vessels, unmanned underwater vehicles, and autonomous underwater vehicles, is important in underwater acoustics. Precise predictions of underwater sound propagation (USP) from such sources clarify the associated propagation behavior and allow the radiated noise level of the source to be assessed. Thus, the primary task for noise control at the preliminary sonar design and maintenance stages is to develop accurate USP predictions. Early work on predicting USP from a structural source in free space considered acoustic radiation spreading without interference from boundary reflections. However, the structural source often operates in shallow water. Complex environments further complicate the USP from structural sources, as the URN becomes coupled with waveguide physics, such as boundary reflections, refraction from sound speed profiles (SSPs), and even modal coupling effects from internal waves. Driven by a recognition of the increasing demands for sonar performance assessments in complex oceans, there has been increasing interest in predicting USP from a structural source in complex shallow-water environments.Zou et al. (2020); Jiang et al. (2020); Jia-xi et al. (2021); Huang et al. (2019a,b); Petris et al. (2022); Wu et al. (2022)

Generally, USP predictions from structural sources require the structural vibration response to be integrated with the USP computations based on the acoustic radiation from the source. The former relies on either analytical or fully numerical approaches, such as the finite element (FE) method, while the latter is essentially an exterior Helmholtz problem, typically solved by the Helmholtz–Kirchhoff integral (H-KI) approach. Coupled FE/H-KI computations have been used for USP from structural sources such as underwater force-driven elastic structures,Zou et al. (2020); Jiang et al. (2020); Jia-xi et al. (2021); Huang et al. (2019a,b); Petris et al. (2022) underwater pile drivers,Peng et al. (2021) and surface vessels.Wu et al. (2022) This coupled computation scheme often utilizes the FE method to compute the

---

\*Corresponding author

 bin\_wang@sjtu.edu.cn (B. Wang)

ORCID(s):

<sup>1</sup>Also at: Department of Naval Architecture and Ocean Engineering Shanghai Jiao Tong University, Shanghai, 200240, P. R. China

distribution of normal particle velocities and sound pressures on an enclosure surrounding the source, over which the H-KI is then implemented to solve the exterior Helmholtz problem. One attractive aspect of this approach is that the geometry of the source is arbitrary in the computations. Nevertheless, the coupled FE/H-KI computations conventionally handle range-independent USP because it relies on an efficient evaluation of Green's function in ideal shallow water with parallel boundaries. Complex shallow-water environments, such as range-dependent seabeds and sound speed inhomogeneities, further complicate the corresponding Green's function, thus dramatically increasing the numerical cost.

This article describes a computation scheme for predicting USP from a structural source in complex shallow water by directly monitoring the normal displacements on the source surface. In this way, the prediction of USP can be implemented not only at the computational level, but also in practice by on-site measurements of structural vibration responses with known information about the shallow-water environment. To achieve this goal, the FE method is employed to compute the structural vibration response. The FE method is chosen because it outperforms other approaches in terms of versatility for the various materials and geometries considered in the simulations, providing simulation scenarios close to reality. Isakson and Chotiros (2011); Isakson et al. (2014) An appropriate USP model is required to incorporate the FE method for propagating the structural-acoustic radiation through a nonuniform waveguide. This model should be capable of handling both the varying waveguide boundaries and the sound speed inhomogeneities in order to provide as realistic a shallow sea as possible.

Classical USP models include the coupled normal mode (CNM), parabolic equation (PE), ray tracing, finite difference (FD) method, FE method, and spectral element method (SEM). CNM is a powerful tool for investigating waveguide physics. Jensen et al. (2011); Decourcy and Duda (2020); Tu et al. (2022); Petnikov et al. (2022) It divides the range-dependent waveguide into range-independent segments (step-wise approximations), and then couples all segments by imposing boundary conditions across the interfaces between each pair of segments. A global coupling matrix is then formed, by which the unknown modal coupling coefficients can be solved. Although simple source excitations can be considered in CNM, those with complex structures and excitations may be difficult to handle if their modal expansion coefficients are non-analytical. With the help of the paraxial approximation to the Helmholtz equation, PE achieves numerical efficiency by ignoring the back-scattering from the waveguide, making it suitable for handling both two- and three-dimensional (2D/3D) problems. Collins and Evans (1992); Sturm (2016); CA Oliveira and Lin (2019); Oliveira et al. (2021) PE has no limitations on the source type, as long as the associated initial field can be computed. Nevertheless, additional numerical treatment, such as the FE model covering the whole waveguide cross-section, may be required to obtain such an initial field, which is then used to solve the differential equations involved in PE. Jensen et al. (2011) Moreover, the approximations inherent in PE may lead to inaccurate USP from structural sources in strongly range-dependent shallow water at arbitrary ranges. Jensen et al. (2011) As one of the earliest methods to be applied to interpret USP behavior from the perspective of geometric acoustics, ray tracing relies on a series expansion of the solution to the Helmholtz equation (high-frequency approximation). Jensen et al. (2011) Recent work on this method Porter (2019) has demonstrated its capability to interpret realistic 3D propagation behaviors found in experimental data. However, finding eigenrays is complicated in the case of complex structural sources and topographies, especially in 3D scenarios. Additionally, ray tracing fails to capture detailed sound fields accurately when the bottom derivatives are discontinuous. Porter (2019)

Approaches based on volume discretization, such as FD, Liu et al. (2021) FE, Isakson and Chotiros (2011); Isakson et al. (2014) and SEM, Cristini and Komatisch (2012); Bottero et al. (2016, 2018) are fully customized in terms of material properties and the geometry of the computation domain, thus enabling USP predictions from arbitrary sources in complex environments. The FD and FE results converge to the wave equation's exact solution under appropriate discretization schemes. Restricted by computation power, however, the problem size treated in FD and FE is typically hundreds of acoustic wavelengths. FD and FE may require computer clusters or supercomputers to solve large-scale USP problems, especially in 3D. The repetitive discretization and meshing make FD and FE unwieldy for Monte Carlo simulations or parametric sweeps when optimizing the sonar performance at the preliminary design stage. Compared with approaches based on volume discretization, boundary integral-based methods (BI-M), such as the boundary element method (BEM) Godinho et al. (2001); Pereira et al. (2010); Li et al. (2019) and the equivalent source method (ESM), can theoretically reach similar numerical precision at a reasonable numerical cost by only discretizing the corresponding boundaries, rather than the whole computational domain. Within the framework proposed by Awai et al., Abawi and Porter (2007) the capability of the ESM-based USP model for scattering from water surfaces, refractions by SSPs, and even fully 3D large-scale problems was recently extended by He et al. He et al. (2020, 2021b,a)

The ESM-based USP model inherits all of the advantages of BEM-based models, but circumvents the singularity resulting from the Green's function, resulting in simpler numerical implementations.

This article proposes a coupled FE/equivalent source (ES) computation scheme for predicting the range-dependent USP from a structural source in complex shallow-water environments. A coupled vibroacoustic FE/ES analysis replaces the structural-acoustic radiation with a set of ESs, in which the FE method computes the structural vibration response, and the free-field ESM couples these responses with the FE computation to reproduce the structural-acoustic radiation at arbitrary spatial positions. Next, a waveguide-field ES computation is performed using the incident-field quantities evaluated by the coupled vibroacoustic FE/ES analysis, and the structural-acoustic radiation is propagated through the shallow-water waveguide. A novel multilayer acoustic–elastic ESM (MLA-EESM) is developed to extend the ESM-based USP model, allowing sound speed inhomogeneities and range-dependent elastic seabeds to be accommodated. MLA-EESM is integrated into the proposed scheme to predict the 2D range-dependent USP from a vibrating infinite cylindrical shell. These simulations demonstrate the interactions of structural-acoustic radiation with complex 2D topographies and internal solitary waves. Parameter sweeps are performed to analyze the validity of an effective complex density fluid model (ECDFM) Zhang and Tindle (1995) for calculating the waveguide field excited by a structural source. With the ECDFM imitating the unconsolidated seabed, a 3D fluid USP model, namely pre-corrected fast Fourier transform-accelerated ESM (PFFT-ESM), He et al. (2021a) is combined with the coupled vibroacoustic FE/ES analysis. This allows the 3D USP from a vibrating shell in shallow water overlying double seamounts to be predicted with reduced computational complexity. Finally, the numerical efficiency of the proposed coupled FE/ES computation scheme is discussed. The remainder of this paper is organized as follows. Section 2 derives the formulae used in the proposed methods, before Sec. 3 presents the results of numerical simulations. Finally, the conclusions to this study are summarized in Sec. 4.

## 2. Methods

Before predicting the range-dependent USP from a structural source, we must model the vibroacoustics of an elastic object. The FE model is sufficiently versatile for the various materials and geometries treated in the simulations and is thus used to calculate the structural vibration response associated with the structural-acoustic radiation. After evaluating the structural vibration response, a free-field ESM Koopmann et al. (1989) is used to couple this response with the FE computation, solving the Helmholtz exterior problem by replacing the structural-acoustic radiation with the superposition of fields generated by a set of ESs within the source. The established FE/ES analyses are then used to evaluate the boundary field, which is required by an ESM-based USP model (described in Sec. 2.2) to propagate the acoustic radiation in a given shallow-water environment. Also, this means that the range-dependent USP from the structural source can be predicted by monitoring the normal displacement over the structure's surface once the shallow-water environment is known.

### 2.1. Coupled finite element/equivalent source analyses for vibroacoustics

As shown in Fig. 1, we describe the vibroacoustic problem as an elastic structure submerged into an unbounded, homogeneous fluid, where the structural vibration domain  $\Omega_{str}$  and the acoustic radiation domain  $\Omega_{acs}$  are represented using FEs and ESs, respectively, with the interface  $\Gamma'_{str-acs}$  coupling these two parts. The equations of motion for coupled FE/ES analyses can be written as Fahline (2021)

$$[\mathbf{K} + j\omega\mathbf{D} - \omega^2\mathbf{M}]\mathbf{u}_{nod} = \mathbf{f}_{ext} + \mathbf{f}_{acs}, \quad (1)$$

where  $\mathbf{K}$ ,  $\mathbf{D}$ , and  $\mathbf{M}$  are the stiffness, damping, and mass matrices,  $\mathbf{u}_{nod}$  is the vector of nodal displacements,  $\mathbf{f}_{ext}$  is the external nodal forces,  $\mathbf{f}_{acs}$  is the fluid loading induced by sound pressures, and  $\omega$  is the angular frequency.

ESM uses a set of ESs over a conformal surface  $\Gamma'_{str-acs}$  within the vibrating structure to generate the same radiations from the structure Koopmann et al. (1989). The exterior sound pressure at  $\mathbf{r}$  is thus an integral of the fields produced by all ESs Koopmann et al. (1989)

$$p_{acs}(\mathbf{r}) = j\rho_w\omega \int_{\Gamma'_{st-a}} s_{acs}(\mathbf{r}') G^{\Phi_w}(\mathbf{r}, \mathbf{r}') d\Gamma'_{str-acs}, \quad (2)$$

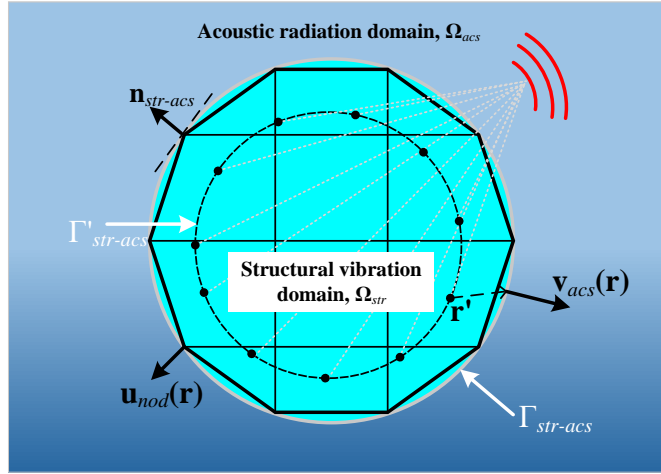


**Figure 1:** Schematic of the coupled vibroacoustic FE/ES analyses.

where  $p_{acs}$  is the nodal sound pressure,  $s_{acs}$  is the ES strength,  $\rho_w$  is the water density, and  $G^{\Phi_w}(\mathbf{r}, \mathbf{r}')$  is the free-field Green's function given by Jensen et al. (2011)

$$G^{\Phi_w}(\mathbf{r}, \mathbf{r}') = \begin{cases} \frac{j}{4} H_0^{(2)}(k_w |\mathbf{r} - \mathbf{r}'|), & 2D \\ \frac{\exp(-jk_w |\mathbf{r} - \mathbf{r}'|)}{4\pi |\mathbf{r} - \mathbf{r}'|}, & 3D \end{cases} \quad (3)$$

where  $H_0^{(2)}$  is the zero-order Hankel function of second kind,  $k_w$  is the wavenumber in water. Discretization of the superposition integral gives

$$\mathbf{p}_{acs} = j\rho_w \omega \mathbf{G}^{\Phi_w} \mathbf{s}_{acs}. \quad (4)$$

Here,  $\mathbf{p}_{acs}$  represents the vector of nodal sound pressures. We now consider the nodal normal velocity  $\mathbf{v}_{acs}$  and write  $\mathbf{v}_{acs}$  in terms of ES amplitudes, this yields Koopmann et al. (1989)

$$\mathbf{v}_{acs} = \mathbf{G}^{v_w} \mathbf{s}_{acs}, \quad (5)$$

where the transfer matrix  $\mathbf{G}^{v_w} = \nabla \mathbf{G}^{\Phi_w} \cdot \hat{\mathbf{n}}_{str-accs}$ , with  $\hat{\mathbf{n}}_{str-accs}$  denoting the outward normal vector to  $\Gamma_{str-accs}$ . Substituting Eq. (5) back into Eq. (4) yields

$$\mathbf{p}_{acs} = j\rho_w \omega \mathbf{G}^{\Phi_w} \mathbf{G}^{v_w - 1} \mathbf{v}_{acs}. \quad (6)$$

We then enforce the following continuity constraints across  $\Gamma_{str-accs}$  to couple the vibration and radiation Fahline (2021)

$$\begin{cases} \mathbf{f}_{acs} = \mathbf{F} \mathbf{p}_{acs}, \\ \mathbf{v}_{acs} = j\omega \mathbf{U} \mathbf{u}_{nod}, \end{cases} \quad (7)$$

where  $\mathbf{F}$ , the conversion matrix of sound pressure, transfers nodal values from the fluid to the structure, and  $\mathbf{U}$  is the conversion matrix of displacement transferring nodal values from the structure to the fluid. By substituting Eq. (7) back into Eqs. (6) and (1), a coupled FE/ES equation is given by

$$\begin{bmatrix} \mathbf{K} + j\omega \mathbf{D} - \omega^2 \mathbf{M} & -\mathbf{F} \\ -\rho_w \omega^2 \mathbf{G}^{\Phi_w} \mathbf{G}^{v_w - 1} \mathbf{U} & -\mathbf{E} \end{bmatrix} \begin{bmatrix} \mathbf{u}_{nod} \\ \mathbf{p}_{acs} \end{bmatrix} = \begin{bmatrix} \mathbf{f}_{ext} \\ 0 \end{bmatrix}. \quad (8)$$

After solving the coupled equation for the nodal displacements, the ES calculations can solve radiations at any field points in the acoustic domain  $\Omega_{acs}$ . This feature of the described FE/ES analyses allows it to incorporate an ESM-based USP model for propagating the structural-acoustic radiation in a complex shallow-water acoustic environment. Here we also give the far-field Green's function by the Fraunhofer approximation for calculating the far-field pattern in the free field:

$$G^{\Phi_f}(\mathbf{r}, \mathbf{r}') = \begin{cases} \sqrt{\frac{1}{2\pi k_w}} e^{-j\pi/4} e^{jk_w(x' \cos \psi + z' \sin \psi)}, & 2D \\ \frac{1}{4\pi} e^{jk_w(x' \cos \theta \cos \psi + y' \cos \theta \sin \psi + z' \sin \theta)}, & 3D \end{cases} \quad (9)$$

where  $\theta$  and  $\psi$  are the azimuth and elevation angles with respect to the acoustic center of the vibrating structure.

Note that the presented coupled FE/ES analyses assume the vibrating structure to be submerged by an unbound fluid, meaning that the effects of waveguide boundaries (multiple scattering between the boundary and structure) on vibroacoustic behaviors are neglected. Although such waveguide-boundary effects can be taken into account by introducing the waveguide Green's function into the coupled equation given by Eq. (8) (equivalent to additional mass loading), this issue is out of the scope of this article and is not addressed here as we mainly focus on more general situations when the underwater vibrating structure operates away from the sea surface and seafloor. For example, a submarine needs to dive over hundreds of meters to prevent it from being detected by its enemy, simultaneously keeping a safe distance from the seafloor to avoid being damaged by accidentally hitting on seamounts and other complex topographies. Also, UUV or ROV often operate at a deep depth for oceanic resource explorations and navy activities.

## 2.2. Equivalent source computation for propagating acoustic radiations in inhomogeneous shallow-water waveguides

After solving the vibroacoustics of an underwater structure using the coupled FE/ES analyses, we now consider an ES computation for propagating acoustic radiations from the structure in inhomogeneous shallow-water waveguides. An MLA-EESM for 2D range-dependent USP in shallow water with an elastic seabed is first established, followed by a brief introduction of a fully 3D model, PFFT-ESM, incorporating an ECDFM Zhang and Tindle (1995) for 3D range-dependent USP in shallow water with a low-shear-speed elastic seabed. The ESM-based USP model has no limitations on the source type and is thus very suitable for considering sound fields excited by structural and multiple sources.

### 2.2.1. Multilayer acoustic–elastic equivalent source method for 2D range-dependent sound propagation in shallow water with an elastic seabed

As shown in Fig. 2, we consider a 2D range-dependent waveguide of  $I$  fluid layers overlying an elastic seabed. The sound speed and density of the  $i$ -th fluid layer are  $c_{w_i}$  and  $\rho_{w_i}$  ( $i = 1, 2, \dots, I$ ), respectively. The compressional and shear wave speeds of the elastic seabed are  $c_p$  and  $c_{sh}$ , respectively, and the seabed density is  $\rho_s$ . Herein,  $\mathbf{r}_{b_0}$  denotes the position of the water surface, and  $\mathbf{r}_{b_i}$  represents the position of the interface between the  $i$ -th layer and its lower layer. The Helmholtz equations governing the scalar potential  $\Phi_{w_i}(\mathbf{r})$  in water and the scalar potential  $\Phi_p(\mathbf{r})$  and shear potential  $\Psi_{sh}(\mathbf{r})$  in the seabed are Jensen et al. (2011)

$$[\nabla^2 + k_{w_i}^2] \Phi_{w_i}(\mathbf{r}) = 0, \mathbf{r} \in \text{water} \quad (10a)$$

$$[\nabla^2 + k_p^2] \Phi_p(\mathbf{r}) = 0, \mathbf{r} \in \text{sediment} \quad (10b)$$

$$[\nabla^2 + k_{sh}^2] \Psi_{sh}(\mathbf{r}) = 0, \mathbf{r} \in \text{sediment} \quad (10c)$$

where  $\mathbf{r} = (x, z)$  is the position vector,  $k_{w_i} = \omega/c_{w_i}$  is the wavenumber in water, and  $k_p = \omega/c_p$  and  $k_{sh} = \omega/c_{sh}$  are the compressional and shear wavenumbers in the seabed, respectively. The pressure-release boundary condition at the

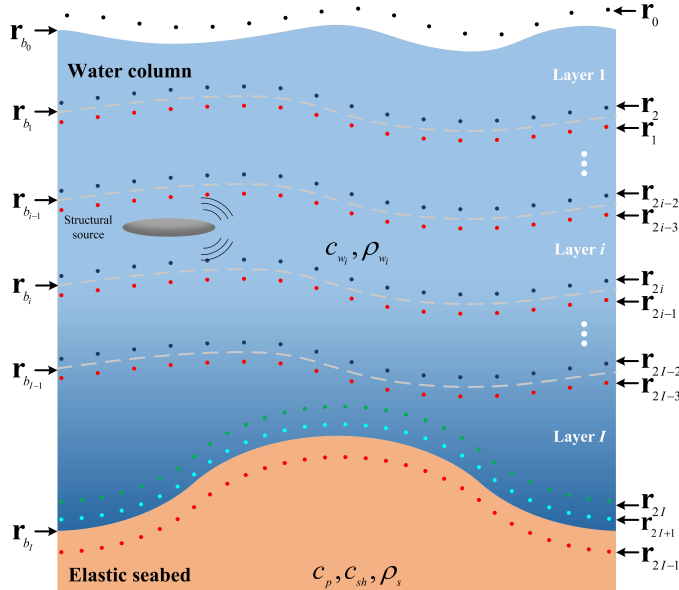


**Figure 2:** Schematic of multilayer acoustic–elastic equivalent source method, with the black, white, and red circles denoting those ESs replacing the field reflected by the sea surface, the upper layer, and the lower layer, respectively. The green and cyan circles represent those ESs producing the compressional and shear potentials in the seabed, respectively.

water surface, the continuity of pressure and normal displacement across the interface between two adjacent layers, the continuity of the normal stress across the seabed interface, and the zero tangential stress at the seabed interface can be expressed as

$$\left\{ \begin{array}{ll} p(\mathbf{r}_{b_0}) = 0, & (i = 0) \\ p(\mathbf{r}_{b_i})|_- = p(\mathbf{r}_{b_i})|_+, & (1 \leq i \leq I - 1) \\ \hat{\mathbf{n}} \cdot \mathbf{u}(\mathbf{r}_{b_i})|_- = \hat{\mathbf{n}} \cdot \mathbf{u}(\mathbf{r}_{b_i})|_+, & (1 \leq i \leq I) \\ \hat{\mathbf{n}} \cdot \boldsymbol{\tau}(\mathbf{r}_{b_I}) \cdot \hat{\mathbf{n}}|_- = -p(\mathbf{r}_{b_I})|_+, & (i = I) \\ \hat{\mathbf{n}} \times [\boldsymbol{\tau}(\mathbf{r}_{b_I}) \cdot \hat{\mathbf{n}}]|_- = 0, & (i = I) \end{array} \right. \quad (11)$$

where  $\mathbf{u}$  is the displacement,  $\boldsymbol{\tau}$  is the stress tensor,  $p$  is the sound pressure, and  $\hat{\mathbf{n}}$  represents the normal unit vector to the corresponding boundary.

The proposed MLA-EESM is developed for range-dependent USP in shallow water over an elastic seabed. This method expresses the solution to Eqs. (10a), (10b), and (10c) as a superposition of basis functions (Green's functions) with unknown coefficients. The coefficients are determined by imposing the boundary conditions defined in Eq. (11). Herein, the scalar and shear potential Green's functions,  $G_{\Phi_{w_i,p}}$  and  $G_{\Psi_{sh}}$ , satisfy Jensen et al. (2011)

$$[\nabla^2 + k_{w_i}^2]G^{\Phi_{w_i}}(\mathbf{r}, \mathbf{r}') = \delta(\mathbf{r} - \mathbf{r}'), \quad (12a)$$

$$[\nabla^2 + k_p^2]G^{\Phi_p}(\mathbf{r}, \mathbf{r}') = \delta(\mathbf{r} - \mathbf{r}'), \quad (12b)$$

$$[\nabla^2 + k_{sh}^2]G^{\Psi_{sh}}(\mathbf{r}, \mathbf{r}') = \delta(\mathbf{r} - \mathbf{r}'), \quad (12c)$$

with the 2D solutions Jensen et al. (2011)

$$\left\{ \begin{array}{l} G^{\Phi_{w_i}}(\mathbf{r}, \mathbf{r}') = \frac{j}{4} H_0^{(2)}(k_{w_i} |\mathbf{r} - \mathbf{r}'|), \\ G^{\Phi_p}(\mathbf{r}, \mathbf{r}') = \frac{j}{4} H_0^{(2)}(k_p |\mathbf{r} - \mathbf{r}'|), \\ G^{\Psi_{sh}}(\mathbf{r}, \mathbf{r}') = \frac{j}{4} H_0^{(2)}(k_{sh} |\mathbf{r} - \mathbf{r}'|). \end{array} \right. \quad (13)$$

where  $\mathbf{r}'$  is the position of the point source.

The displacement vectors in water and the elastic seabed are given by Abawi and Porter (2007)

$$\mathbf{u}(\mathbf{r}) = \left\{ \begin{array}{ll} \frac{1}{\omega^2 \rho_{w_i}} \nabla \Phi_{w_i}(\mathbf{r}), & \mathbf{r} \in \text{water} \\ \frac{1}{\omega^2 \rho_s} \left[ \nabla \Phi_p(\mathbf{r}) + \nabla \times [0, \Psi_{sh}(\mathbf{r}), 0] \right], & \mathbf{r} \in \text{sediment} \end{array} \right. \quad (14)$$

In the elastic seabed, the relation between the stress tensor and the displacement in 2D is given by Abawi and Porter (2007)

$$\left\{ \begin{array}{l} \boldsymbol{\tau}_{xx} = (\lambda_{sh} + 2\mu) \frac{\partial \mathbf{u}_x}{\partial x} + \lambda_{sh} \frac{\partial \mathbf{u}_z}{\partial z}, \\ \boldsymbol{\tau}_{xz} = \mu \left( \frac{\partial \mathbf{u}_x}{\partial z} + \frac{\partial \mathbf{u}_z}{\partial x} \right), \\ \boldsymbol{\tau}_{zz} = (\lambda_{sh} + 2\mu) \frac{\partial \mathbf{u}_z}{\partial z} + \lambda_{sh} \frac{\partial \mathbf{u}_x}{\partial x}, \end{array} \right. \quad (15)$$

where  $\lambda_{sh} = \rho_s(c_p^2 - 2c_{sh}^2)$  and  $\mu = \rho_s c_{sh}^2$  are the Lame constants, and

$$\left\{ \begin{array}{l} \mathbf{u}_x = \frac{1}{\omega^2 \rho_s} \left( \frac{\partial \Phi_p}{\partial x} - \frac{\partial \Psi_{sh}}{\partial z} \right), \\ \mathbf{u}_z = \frac{1}{\omega^2 \rho_s} \left( \frac{\partial \Phi_p}{\partial z} + \frac{\partial \Psi_{sh}}{\partial x} \right), \end{array} \right. \quad (16)$$

while in the water column, the displacement vector becomes

$$\left\{ \begin{array}{l} \mathbf{u}_x = \frac{1}{\omega^2 \rho_{w_i}} \frac{\partial \Phi_{w_i}}{\partial x}, \\ \mathbf{u}_z = \frac{1}{\omega^2 \rho_{w_i}} \frac{\partial \Phi_{w_i}}{\partial z}. \end{array} \right. \quad (17)$$

In MLA-EESM, the waveguide field in the top fluid layer ( $i = 1$ ) can be separated into the fields reflected by the surface and by the second fluid layer. In the  $i$ -th layer ( $i > 1$ ), the sound field is the summation of the fields reflected by the  $i-1$ -th and the  $i+1$ -th layers. Accordingly, a set of ESs is placed above the sea surface at  $\mathbf{r}_0$ , replacing the surface-reflected field. In the  $i$ -th fluid layer ( $1 < i$ ), two sets of ESs are utilized, one above the layer's upper boundary at  $\mathbf{r}_{2i-2}$  and the other below the layer's upper boundary at  $\mathbf{r}_{2i-1}$ , replacing the fields reflected by the  $i-1$ -th and  $i+1$ -th layers, respectively. In addition, the compressional and shear potentials require two sets of ESs above the elastic seabed to produce the equivalent field in the seabed. Those representing the scalar and shear potentials are placed at  $\mathbf{r}_{2I}$  and  $\mathbf{r}_{2I+1}$ , respectively. In this way, the sound pressure and normal displacement in the water column can be written as Abawi and Porter (2007)

$$\left\{ \begin{array}{l} p_{w_i}(\mathbf{r}) = \sum_{n=1}^N G^{\Phi_{w_i}}(\mathbf{r}, \mathbf{r}_{2i-2(n)}) s_{2i-2(n)} + \sum_{n=1}^N G^{\Phi_{w_i}}(\mathbf{r}, \mathbf{r}_{2i-1(n)}) s_{2i-1(n)}, \\ u_{w_i}(\mathbf{r}) = \sum_{n=1}^N G^{u_{w_i}}(\mathbf{r}, \mathbf{r}_{2i-2(n)}) s_{2i-2(n)} + \sum_{n=1}^N G^{u_{w_i}}(\mathbf{r}, \mathbf{r}_{2i-1(n)}) s_{2i-1(n)}, \end{array} \right. \quad (18)$$

the normal displacements in the seabed can be written as

$$\left\{ \begin{array}{l} u_p(\mathbf{r}) = \sum_{n=1}^N G^{u_p}(\mathbf{r}, \mathbf{r}_{2I(n)}) s_{2I(n)}, \\ u_{sh}(\mathbf{r}) = \sum_{n=1}^N G^{u_{sh}}(\mathbf{r}, \mathbf{r}_{2I+1(n)}) s_{2I+1(n)}, \end{array} \right. \quad (19)$$

and the stress tensors in the seabed are given by

$$\left\{ \begin{array}{l} \tau_{p_{nor}}(\mathbf{r}) = \sum_{n=1}^N G^{\tau_{p_{nor}}}(\mathbf{r}, \mathbf{r}_{2I(n)}) s_{2I(n)}, \\ \tau_{sh_{nor}}(\mathbf{r}) = \sum_{n=1}^N G^{\tau_{sh_{nor}}}(\mathbf{r}, \mathbf{r}_{2I+1(n)}) s_{2I+1(n)}, \\ \tau_{p_{tan}}(\mathbf{r}) = \sum_{n=1}^N G^{\tau_{p_{tan}}}(\mathbf{r}, \mathbf{r}_{2I(n)}) s_{2I(n)}, \\ \tau_{sh_{tan}}(\mathbf{r}) = \sum_{n=1}^N G^{\tau_{sh_{tan}}}(\mathbf{r}, \mathbf{r}_{2I+1(n)}) s_{2I+1(n)}, \end{array} \right. \quad (20)$$

where the subscript  $(n)$  specifies the  $n$ -th ES of each set,  $s_n$  is its amplitude, and  $N$  is the total number of each set of ESs. Herein,  $p_{w_i}$  and  $u_{w_i}$  denote the sound pressure and the normal displacement in the  $i$ -th fluid layer, respectively. In the elastic seabed,  $u_p$  and  $u_{sh}$  denote the normal components of the compressional and shear displacements, respectively,  $\tau_{p_{nor}}$  and  $\tau_{sh_{nor}}$  denote the normal components of the compressional and shear stress tensors, respectively, and  $\tau_{p_{tan}}$  and  $\tau_{sh_{tan}}$  denote the tangential components of the compressional and shear stress tensors, respectively. According to Eq. (14), the normal-displacement Green's functions,  $G^{u_{w_i}}(\mathbf{r}, \mathbf{r}')$ ,  $G^{u_p}(\mathbf{r}, \mathbf{r}')$ , and  $G^{u_{sh}}(\mathbf{r}, \mathbf{r}')$ , have the following mathematical expressions

$$\left\{ \begin{array}{l} G^{u_{w_i}}(\mathbf{r}, \mathbf{r}') = \frac{1}{\omega^2 \rho_{w_i}} \left[ \hat{\mathbf{n}}_x \frac{\partial}{\partial x} + \hat{\mathbf{n}}_z \frac{\partial}{\partial z} \right] G^{\Phi_{w_i}}(\mathbf{r}, \mathbf{r}'), \\ G^{u_p}(\mathbf{r}, \mathbf{r}') = \frac{1}{\omega^2 \rho_s} \left[ \hat{\mathbf{n}}_x \frac{\partial}{\partial x} + \hat{\mathbf{n}}_z \frac{\partial}{\partial z} \right] G^{\Phi_p}(\mathbf{r}, \mathbf{r}'), \\ G^{u_{sh}}(\mathbf{r}, \mathbf{r}') = \frac{1}{\omega^2 \rho_s} \left[ -\hat{\mathbf{n}}_x \frac{\partial}{\partial z} + \hat{\mathbf{n}}_z \frac{\partial}{\partial x} \right] G^{\Psi_{sh}}(\mathbf{r}, \mathbf{r}'), \end{array} \right. \quad (21)$$

while the normal and tangential components of the stress tensors,  $G^{\tau_{p_{nor}}}(\mathbf{r}, \mathbf{r}')$ ,  $G^{\tau_{sh_{nor}}}(\mathbf{r}, \mathbf{r}')$ ,  $G^{\tau_{p_{tan}}}(\mathbf{r}, \mathbf{r}')$ , and  $G^{\tau_{sh_{tan}}}(\mathbf{r}, \mathbf{r}')$ , are given by

$$\left\{ \begin{array}{l} G^{\tau_{p_{nor}}}(\mathbf{r}, \mathbf{r}') = \frac{1}{\omega^2 \rho_s} \left[ \hat{\mathbf{n}}_x^2 A_1 + \hat{\mathbf{n}}_z^2 B_1 + 2\hat{\mathbf{n}}_x \hat{\mathbf{n}}_z C_1 \right], \\ G^{\tau_{sh_{nor}}}(\mathbf{r}, \mathbf{r}') = \frac{1}{\omega^2 \rho_s} \left[ \hat{\mathbf{n}}_x^2 A_2 + \hat{\mathbf{n}}_z^2 B_2 + 2\hat{\mathbf{n}}_x \hat{\mathbf{n}}_z C_2 \right], \\ G^{\tau_{p_{tan}}}(\mathbf{r}, \mathbf{r}') = \frac{1}{\omega^2 \rho_s} \left[ (\hat{\mathbf{n}}_x^2 - \hat{\mathbf{n}}_z^2) C_1 + \hat{\mathbf{n}}_z \hat{\mathbf{n}}_x (B_1 - A_1) \right], \\ G^{\tau_{sh_{tan}}}(\mathbf{r}, \mathbf{r}') = \frac{1}{\omega^2 \rho_s} \left[ (\hat{\mathbf{n}}_x^2 - \hat{\mathbf{n}}_z^2) C_2 + \hat{\mathbf{n}}_z \hat{\mathbf{n}}_x (B_2 - A_2) \right], \end{array} \right. \quad (22)$$

where

$$\left\{ \begin{array}{l} A_1 = \left[ (\lambda_{sh} + 2\mu) \frac{\partial^2}{\partial x^2} + \lambda_{sh} \frac{\partial^2}{\partial z^2} \right] G^{\Phi_p}(\mathbf{r}, \mathbf{r}'), \\ B_1 = \left[ (\lambda_{sh} + 2\mu) \frac{\partial^2}{\partial z^2} + \lambda_{sh} \frac{\partial^2}{\partial x^2} \right] G^{\Phi_p}(\mathbf{r}, \mathbf{r}'), \\ C_1 = 2\mu \frac{\partial^2 G^{\Phi_p}(\mathbf{r}, \mathbf{r}')}{\partial x \partial z}, \\ A_2 = \left[ -(\lambda_{sh} + 2\mu) \frac{\partial^2}{\partial x \partial z} + \lambda_{sh} \frac{\partial^2}{\partial z \partial x} \right] G^{\Psi_{sh}}(\mathbf{r}, \mathbf{r}'), \\ B_2 = \left[ (\lambda_{sh} + 2\mu) \frac{\partial^2}{\partial z \partial x} - \lambda_{sh} \frac{\partial^2}{\partial x \partial z} \right] G^{\Psi_{sh}}(\mathbf{r}, \mathbf{r}'), \\ C_2 = \mu \left[ -\frac{\partial^2}{\partial z^2} + \frac{\partial^2}{\partial x^2} \right] G^{\Psi_{sh}}(\mathbf{r}, \mathbf{r}'). \end{array} \right. \quad (23)$$

In the above equations,  $\hat{\mathbf{n}}_x$  and  $\hat{\mathbf{n}}_z$  are the horizontal and vertical components of the unit normal vector  $\hat{\mathbf{n}}$ . For each interface at  $r_{b_i}$ , consider a vector of field points  $r_{b_i}(1), r_{b_i}(2), \dots, r_{b_i}(N)$ . After substituting for the pressure, displacement, and stress tensor in the boundary conditions given by Eq. (11) in terms of the ES amplitudes, this yields a linear system coupling all fields generated by  $2I + 2$  sets of ESs

$$[\mathbf{G}]\{\mathbf{s}\}^T = \{\mathbf{e}\}^T, \quad (24)$$

where  $\{\mathbf{s}\}^T$  is the unknown amplitude vector given by

$$\{\mathbf{s}\}^T = \{\mathbf{s}_0, \mathbf{s}_1, \mathbf{s}_2, \mathbf{s}_3, \dots, \mathbf{s}_{2i-2}, \mathbf{s}_{2i-1}, \mathbf{s}_{2i}, \mathbf{s}_{2i+1}, \dots, \mathbf{s}_{2I-2}, \mathbf{s}_{2I-1}, \mathbf{s}_{2I}, \mathbf{s}_{2I+1}\}^T, \quad (25)$$

and right-hand-side vector  $\{\mathbf{e}\}^T$  is the incident field quantity composed of

$$\{\mathbf{e}\}^T = \{\mathbf{e}_0, \mathbf{e}_1, \mathbf{e}_2, \dots, \mathbf{e}_{2i-1}, \mathbf{e}_{2i}, \dots, \mathbf{e}_{2I-1}, \mathbf{e}_{2I}, \mathbf{e}_{2I+1}\}^T. \quad (26)$$

In the above linear system, the global coefficient matrix  $[\mathbf{G}]$  can be written as

$$\left[ \begin{array}{ccccccccc} \mathbf{G}_{0,0}^{\Phi_{w_1}} & \mathbf{G}_{0,1}^{\Phi_{w_1}} & & & & & & & \\ \mathbf{G}_{1,0}^{\Phi_{w_1}} & \mathbf{G}_{1,1}^{\Phi_{w_1}} & -\mathbf{G}_{1,2}^{\Phi_{w_1}} & -\mathbf{G}_{1,3}^{\Phi_{w_1}} & & & & & \\ \mathbf{G}_{1,0}^{\Phi_{w_1}} & \mathbf{G}_{1,1}^{\Phi_{w_1}} & -\mathbf{G}_{1,2}^{\Phi_{w_1}} & -\mathbf{G}_{1,3}^{\Phi_{w_1}} & & & & & \\ \mathbf{G}_{1,0}^{\Phi_{w_1}} & \mathbf{G}_{1,1}^{\Phi_{w_1}} & -\mathbf{G}_{1,2}^{\Phi_{w_1}} & -\mathbf{G}_{1,3}^{\Phi_{w_1}} & & & & & \\ \ddots & \ddots & \ddots & \ddots & & & & & \\ & & & & \mathbf{G}_{i,2i-2}^{\Phi_{w_i}} & \mathbf{G}_{i,2i-1}^{\Phi_{w_i}} & -\mathbf{G}_{i,2i}^{\Phi_{w_{i+1}}} & -\mathbf{G}_{i,2i+1}^{\Phi_{w_{i+1}}} & \\ & & & & \mathbf{G}_{i,2i-2}^{\Phi_{w_i}} & \mathbf{G}_{i,2i-1}^{\Phi_{w_i}} & -\mathbf{G}_{i,2i}^{\Phi_{w_{i+1}}} & -\mathbf{G}_{i,2i+1}^{\Phi_{w_{i+1}}} & \\ & & & & \mathbf{G}_{i,2i-2}^{\Phi_{w_i}} & \mathbf{G}_{i,2i-1}^{\Phi_{w_i}} & -\mathbf{G}_{i,2i}^{\Phi_{w_{i+1}}} & -\mathbf{G}_{i,2i+1}^{\Phi_{w_{i+1}}} & \\ & & & & \ddots & \ddots & \ddots & \ddots & \\ & & & & & & & & \mathbf{G}_{I,2I-2}^{\Phi_{w_I}} & \mathbf{G}_{I,2I-1}^{\Phi_{w_I}} & \mathbf{G}_{I,2I}^{\tau_{p_{nor}}} & \mathbf{G}_{I,2I+1}^{\tau_{sh_{nor}}} \\ & & & & & & & & \mathbf{G}_{I,2I-2}^{\Phi_{w_I}} & \mathbf{G}_{I,2I-1}^{\Phi_{w_I}} & -\mathbf{G}_{I,2I}^{\tau_p} & -\mathbf{G}_{I,2I+1}^{\tau_{ush}} \\ & & & & & & & & \mathbf{G}_{I,2I-2}^{\Phi_{w_I}} & \mathbf{G}_{I,2I-1}^{\Phi_{w_I}} & \mathbf{G}_{I,2I}^{\tau_{p_{tan}}} & \mathbf{G}_{I,2I+1}^{\tau_{sh_{tan}}} \end{array} \right] \quad (27)$$

In the above equations, the bold uppercase letters represent  $N \times N$  transfer matrices with the entries calculated using Eqs. (13), (21), and (22), the bold lowercase letters are the  $1 \times N$  vectors, the subscript  $i,l$  of each transfer matrix specifies the boundary field at  $\mathbf{r}_{b_i}$  produced by ES placed at  $\mathbf{r}_l$ , i.e.,

$$\mathbf{G}_{i,l} = \mathbf{G}(\mathbf{r}_{b_i}, \mathbf{r}_l). \quad (28)$$

For the source producing the incident field in the top fluid layer,  $\{\mathbf{e}\}^T$  has the explicit expression:

$$\{\mathbf{e}\}^T = \{-\mathbf{p}_{inc}(\mathbf{r}_{b_0}), -\mathbf{p}_{inc}(\mathbf{r}_{b_1}), -\mathbf{u}_{inc}(\mathbf{r}_{b_1}), \underbrace{\mathbf{0}, \dots, \mathbf{0}}_{(2I-1) \times \mathbf{0}}\}^T, \quad (29)$$

while for the source placed in the  $i$ -th fluid layer ( $i > 1$ ),  $\mathbf{e}$  becomes

$$\{\mathbf{e}\}^T = \underbrace{\{\mathbf{0}, \dots, \mathbf{0}\}}_{(2i-1) \times \mathbf{0}}, \mathbf{p}_{inc}(\mathbf{r}_{b_{i-1}}), \mathbf{u}_{inc}(\mathbf{r}_{b_{i-1}}), -\mathbf{p}_{inc}(\mathbf{r}_{b_i}), -\mathbf{u}_{inc}(\mathbf{r}_{b_i}), \underbrace{\mathbf{0}, \dots, \mathbf{0}}_{(2I-2i-1) \times \mathbf{0}}\}^T, \quad (30)$$

where  $\mathbf{p}_{inc}$  and  $\mathbf{u}_{inc}$  are the  $1 \times N$  vectors of incident pressures and normal displacements at the corresponding boundary. In this article, these quantities produced by a structural source are calculated using coupled FE/ES analyses introduced in Sec. 2.1. After solving the linear system, the waveguide field in an arbitrary layer can be calculated using Eqs. (18) and (19).

### 2.2.2. Pre-corrected Fast Fourier transform–accelerated equivalent source method for 3D range-dependent sound propagation in shallow water with a low-shear-speed elastic seabed

To obtain a fully 3D ESM-based model for USP over an elastic seafloor with reduced computational complexities, we alternatively use PFFT-ESM to solve 3D USP over an equivalent fluid seabed modeled by ECDFM, which approximates the reflectivity of unconsolidated seabeds.

He *et al.* He et al. (2021a) have demonstrated the ability of PFFT-ESM for fully 3D range-dependent USP over a fluid seabed. Similarly, PFFT-ESM handles sound speed inhomogeneities by dividing the water column into layers and enables structural sources to excite the waveguide field. The linear system coupling all sets of ESs, which provide replacements to the decomposed waveguide field in each fluid layer, is assembled by enforcing the continuities across each interface between two layers. Each set of ESs satisfies 3D Green's functions in PFFT-ESM, and a large-size linear system to be solved is finally obtained. Aiming to save the computational cost of large-size matrix problems in 3D, PFFT-ESM solves the linear system without actually assembling the dense coefficient matrix  $[\mathbf{G}]$ . This is achieved using an iterative solver rather than a direct solver for the linear system and accelerating the computation of matrix–vector product  $[\mathbf{G}]\mathbf{s}$  in each iteration. PFFT is used to accelerate the computation of  $[\mathbf{G}]\mathbf{s}$ , converting the matrix–vector multiplication to a convolution operation by projecting all ESs onto an FFT grid covering each fluid layer. PFFT reduces the computational cost from  $O(N^3)$  required by the direct solver to  $O(N \log N)$  significantly, enabling the large-scale 3D USP problem to be solved on a standard computer. Details of PFFT-ESM can be found in Ref. He et al. (2021a).

Next, we use the ECDFM to imitate the unconsolidated, half-space seabed using an equivalent fluid seabed with a complex density, Zhang and Tindle (1995) reducing the computational complexity for modeling the corresponding shallow-water propagation. This means that PFFT-ESM is used to model USP over a low-shear-speed seabed using the input seabed parameters given by ECDFM. Under the low-grazing angle and low-shear-speed assumptions, the complex density of an equivalent fluid seabed to an unconsolidated seabed is given by Zhang and Tindle (1995)

$$\rho'_s = \rho_s \left[ \left( 1 - \frac{2}{d_1^2} \right)^2 - \frac{j4\sqrt{(1-d_2^2)(d_1^2-1)}}{d_1^4} \right], \quad (31)$$

where  $d_1 = \frac{c_{w_I}}{c_{sh}} - \frac{j\alpha_{sh}c_{w_I}}{\omega}$ , and  $d_2 = \frac{c_{w_I}}{c_p} - \frac{j\alpha_pc_{w_I}}{\omega}$ , with  $\alpha_{sh}$  and  $\alpha_p$  representing the attenuation coefficients of the shear and compressional waves in dB/m, respectively.

When dealing with the waveguide field excited by a structural source, the directionality determines where the dominant propagating energy comes from by weighting the modal amplitudes. When high-order modes propagating at large grazing angles are weighted with the dominant energy, the ECDFM may not be as accurate as for the monopole-point-source excitation for which it was derived due to the low-grazing angle restriction. Discussion on the applicability of ECDFM for a structural source is presented at the end of Sec. 3.1.2.

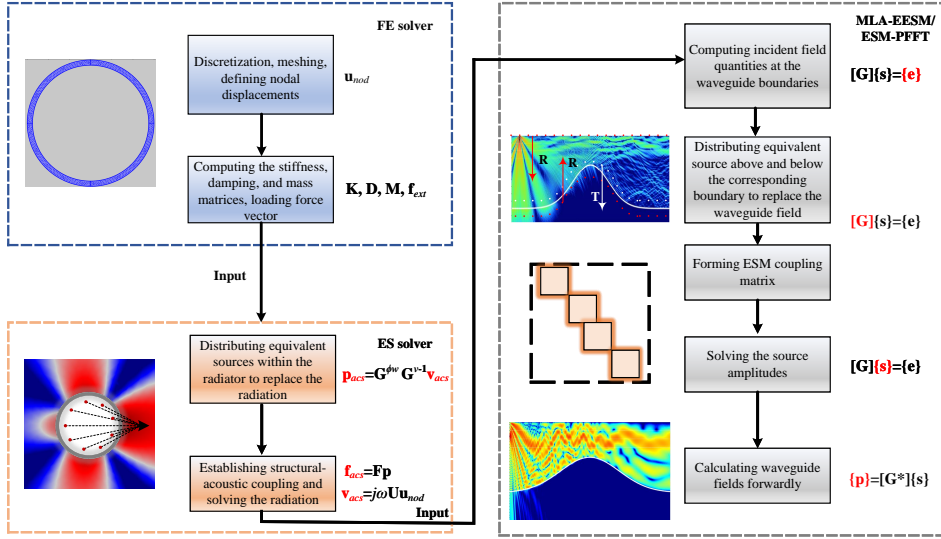


**Figure 3:** Flowchart of coupled FE/ES computations for USP predictions from structural sources in complex shallow water.

### 2.3. Coupled FE/ES computation for modeling underwater sound propagation from a structural source in the range-dependent shallow water waveguide

In summary, the coupled vibroacoustic FE/ES analyses first evaluate an elastic structure's vibration response and then give the incident-field quantities required by the ESM-based USP model. The linear system in Eq. (27) is then assembled according to the procedure described in Sec. 2.2 for a given shallow-water environment. Finally, the unknown vector of the linear system is solved to reproduce the waveguide field, which propagates the structural-acoustic radiation in the shallow-water environment using Eqs. (18) and (19). Fig 3 shows a flowchart of the proposed coupled FE/ES computation scheme.

## 3. Numerical simulations

This section describes a series of numerical simulations to evaluate the performance of the proposed methods. First, to benchmark MLA-EESM and the proposed coupled FE/ES computation scheme, the results are compared with those from an FE model for 2D range-dependent USP from a vibrating infinite cylindrical shell in shallow water overlying an elastic Gaussian seamount and an elastic Gaussian canyon. Next, parametric sweeps are performed to investigate the validity of the ECDFM for modeling the USP from a structural source in shallow water overlying a low-shear-speed seabed. This allows the computational complexity of the corresponding 3D range-dependent USP to be dramatically reduced using a 3D fluid USP model. Finally, simulations are conducted using the 3D range-dependent USP from a vibrating shell in shallow water overlying double unconsolidated seamounts. These simulations are implemented using a 3D fluid UPS model, i.e., PFFT-ESM, with the ECDFM imitating the low-shear-speed seabed.

### 3.1. 2D range-dependent USP from an infinite cylindrical shell

We first consider the 2D range-dependent USP from a force-driven, steel, infinite cylindrical shell overlying an elastic Gaussian seamount in shallow water. Although such a simplified geometry is theoretical and unrealistic, it provides fairly good approximations of the finite cylindrical shell vibrating with only circumferential modes excited and dominated, which is vital for reproducing the vertical directionality of the cylindrical structure at theoretical stages. The FE model is implemented using the commercial COMSOL Multiphysics software. The cylindrical shell has a radius of 6 m and a thickness of 0.1 m. A triangular mesh with a maximum element size of 1/120 the acoustic wavelength is used to discretize the shell, giving a detailed description of the vibration response. Such a meshing scheme guarantees a convergent FE solution Isakson and Chotiros (2011); He et al. (2020, 2021b,a). The shell material is considered to be structural steel with Young's modulus of  $2.09 \times 10^{13}$  Pa, Poisson's ratio of 0.269, and density of 7890 kg/m<sup>3</sup>. The

domain inside the shell is a vacuum. The focal point of a normal force (50 N) is initially loaded at the inner wall of the shell, at (5.9 m, 0 m).

To implement MLA-EESM, each set of ESs is placed on a conformal line offset from the corresponding boundary by the same stand-off distance. The ESs are distributed at the conformal lines with an element length  $\Delta$  between two adjacent sources of  $\lambda/6$  and a stand-off distance  $d_s$  of  $2\Delta$  for the ESs representing the scalar potential and  $\Delta$  for those representing the shear potential. A detailed investigation of the ES configuration used in this study suggests that this provides a reasonable compromise; thus, this configuration is used in all numerical experiments described below.

### 3.1.1. 2D coupled FE/ES analyses for vibro-acoustics

Before calculating the 2D range-dependent USP from the vibrating shell, we test the effectiveness of the coupled FE/ES analyses for vibroacoustics. In replacing the structural-acoustic radiation, 360 ESs are uniformly distributed on a circle of radius 4.8 m within the shell.

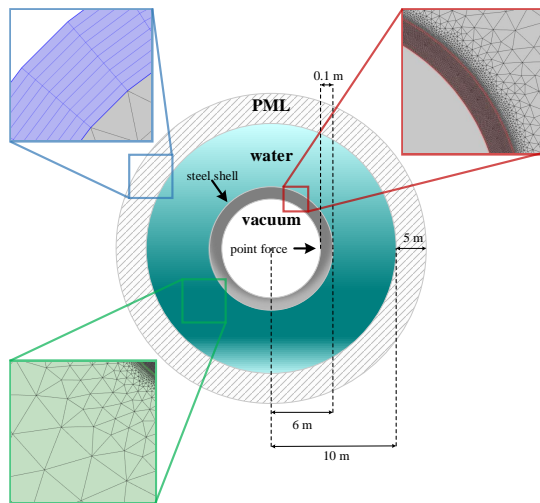


**Figure 4:** Schematic of the FE far-field prediction and the corresponding meshing scheme.

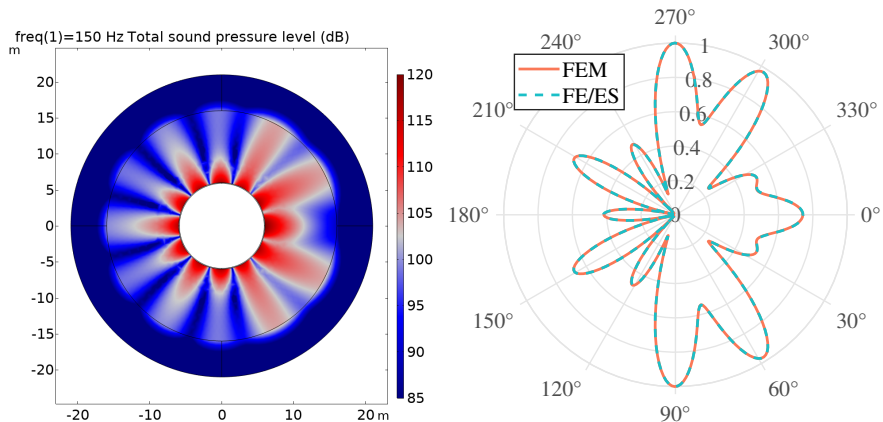


**Figure 5:** The near-field radiation calculated by the FE model (left column) and the far-field pattern (right column) predicted by the coupled vibroacoustic FE/ES analysis (green dotted line) at 150 Hz. The FE result (red solid line) is also given for comparison purposes.

Fig 5 shows the near-field radiation calculated by the FE model and the far-field pattern predicted by the coupled FE/ES analyses at 150 Hz. For comparison purposes, the FE far-field result is also given using the far-field calculation in the COMSOL software (based on the H-KI approach). As for the FE far-field prediction, the solid mechanics

**Table 1**

Parameters of the elastic seabed simulated and of the effective complex density fluid model.

Units	$c_p$ m/s	$\alpha_p$ dB/ $\lambda$	$c_{sh}$ m/s	$\alpha_{sh}$ dB/ $\lambda$	$\rho_s$ g/cm <sup>3</sup>	$\rho'_s$ g/cm <sup>3</sup>
Seabed 1	2400	0.2	1200	0.5	2.1	/
Seabed 2	3000	0.2	1600	0.1	2.1	/
Seabed 3	1950	0.4	600	1	2.1	1.065 – 0.428i
Seabed 4	3000	0.2	1500	0.1	2.4	1.003 – 0.987i

and pressure acoustics modules are used to couple the structural vibration response with the acoustic radiation by establishing an acoustic/solid coupling boundary at the shell surface. Fig 4 shows a diagram of the FE far-field model and the corresponding meshing scheme. Triangular meshes with a maximum element size of 1/6 the acoustic wavelength are used to discretize the circular water domain of radius 10 m. The computation domain is truncated by perfectly matched layers (PMLs), composed of a mapping mesh of 40 layers of thickness 5 m. The far-field prediction is consistent with the FE result, thus confirming the correct configuration of ESs for predicting the 2D range-dependent USP in the next step.

### 3.1.2. 2D waveguide-field ES computation

#### Validation case for shallow water overlying an elastic Gaussian seamount

The coupled vibroacoustic FE/ES analyses give the incident-field quantities required by MLA-EESM (the right-hand-side of the linear system  $\mathbf{G}\mathbf{s} = \mathbf{e}$ ), allowing us to calculate the range-dependent USP from the shell in complex shallow-water environments. Fig 6 shows the shallow-water environment treated in the simulation. The computation domain extends from  $x = -0.1$  km to  $x = 10$  km and from  $z = 0$  m to  $z = -800$  m. The topography of the seabed is a Gaussian seamount, determined by  $z_b(x) = h_0 - h_1 e^{-(x-5000)^2/\delta^2}$ , where  $h_0 = -500$  m,  $h_1 = -250$  m, and  $\delta = 2600$ . In this simulation, two elastic seabeds are tested, labeled Seabed 1 and Seabed 2 in Table 1. The water column is divided into four layers to accommodate the sound speed inhomogeneities. The top three layers form a thermocline layer, and the bottom layer represents the isothermal layer, where the sound speed barely varies with depth. The sound speeds from the top to the bottom water layers are 1524 m/s, 1512 m/s, 1500 m/s, and 1494 m/s, respectively. The cylindrical shell is placed at  $z = -100$  m.

Note that all simulations were performed neglecting the influence of external hydrostatic pressure. Since this article's primary goal is to address the coupling between structural-acoustic radiation with inhomogeneous waveguides, we mainly focus on the propagation characteristic, which is likely to be affected by the far-field pattern of the source. The previous studies showed that hydrostatic pressure's influence on the vibroacoustic behaviors of submerged shells is significant for near-field radiation at low frequencies Pan et al. (2020). However, the far-field radiation remains almost identical with and without the external hydrostatic pressure load Pan et al. (2020). The near-field radiation from the source corresponds to high-order vibration modes, the energy from which couples with the high-order evanescent modes. Nevertheless, the far-field radiation excites low-order propagation modes traveling at shallow grazing angles with the horizontal. Thus its energy, which is barely affected by the hydrostatic pressure, can be trapped and dominated within the waveguide. Other impacts of hydrostatic pressure, such as shifting the structural resonance frequency and suppressing the radiation power Keltie (1986), are out-of-scope of this article and thus are not discussed to save space.

Excellent agreement with the FE results can be observed in Fig. 7, where the transmission loss (TL) is plotted as a function of the horizontal range with a receiver depth of  $-150$  m at 150 Hz, thus confirming the accuracy of the proposed coupled FE/ES computation scheme and MLA-EESM. Fig 8 displays the USP from the cylindrical shell in the whole computation domain, with the right and left columns giving the compressional and shear potentials, respectively. The sediment fields are represented by half of the tensor matrix trace. Due to the modal cut-off associated with the up-slope propagation and the downward refraction by the SSP, the interference pattern becomes weak as the sound wave propagates across the seamount. The apparent energy leakage observed in the seabed confirms the modal cut-off effect. Moreover, the unconsolidated seabed scenario (shear speeds slower than the water speed) exhibits evanescent normal modes, with greater TL than for the consolidated seabed scenario (shear speeds faster than the water speed). Propagating modes are associated with those rays traveling at subcritical grazing angles, and the supercritical sound incidence causes evanescent modes. For the consolidated seabed, two types of perfect internal reflections occur at low grazing angles (long ranges), corresponding to the compressional and shear waves, respectively. The near-perfect

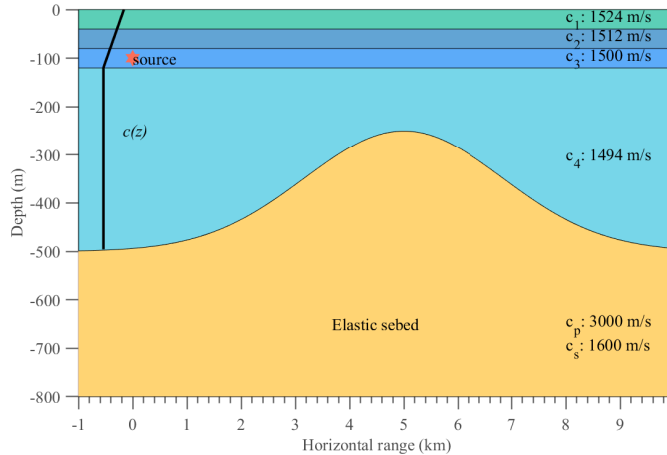


**Figure 6:** Schematic of the shallow-water environment considered in the simulation, with the horizontally stratified water column overlying an elastic Gaussian seamount. The abscissa and ordinate of the plot represent the horizontal range and the depth, respectively.

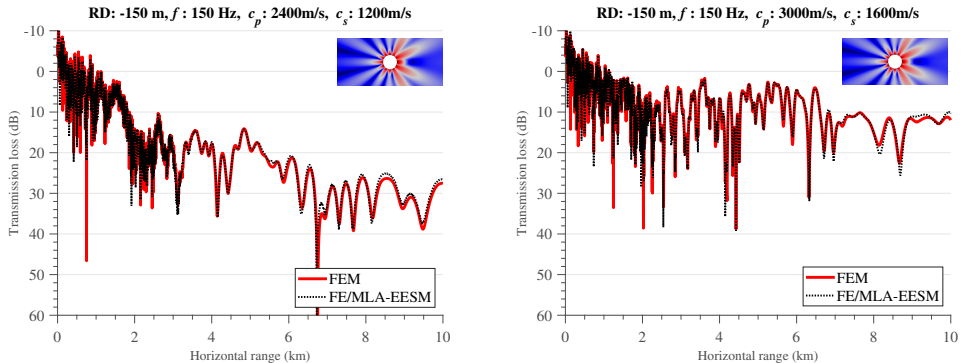


**Figure 7:** Transmission loss comparisons between the FE solutions (red solid line) and the coupled FE/ES computations (black dotted line) in shallow water overlying an elastic Gaussian seamount with a receiver depth of  $z = -150$  m at 150 Hz. Two different seabed properties are considered: the unconsolidated (left column) and consolidated (right column) seabeds. The abscissa and ordinate of these plots represent the horizontal range and transmission loss in dB, respectively.

reflectivity permits the propagating modes to be excited. By contrast, total transmission occurs at the shear-wave intromission angle for the unconsolidated seabed, taking energy out of the system by compressional-to-shear energy conversion. Consequently, the shear wave propagates in the sediment as a plane wave (see the second row of Fig. 8), and the normal mode in water becomes evanescent.

#### Internal wave case

A shallow-water environment with a Gaussian canyon in the presence of internal solitary waves (ISWs) is now considered. The elastic Gaussian canyon is determined by  $z_b(x) = h_0 - h_1 e^{-(x-5000)^2/\delta^2}$ , where  $h_0 = -300$  m,  $h_1 = 250$  m, and  $\delta = 2600$ ; the seabed material is consistent with the consolidated seabed in the previous simulations. Fig 9 shows that the water column is divided into five layers, with the iso-velocity top and bottom layers distinguished at  $z = -130$  m and  $z = -250$  m, respectively. Three layers in the middle represent the internal wave layers, each of which is 40 m thick. The sound speed of the ISWs varies linearly from 1530 m/s to 1494 m/s. The shapes of the ISWs are given by  $75 \operatorname{sech}^2[(x - 2000)/1000]$ . Badiey et al. (2005) The shell is placed at  $z = -150$  m, and is driven by a point force loaded at the right-hand-side wall ( $0^\circ$ ) at 100 Hz.

First, a benchmark is established through comparisons with the FE model. The excellent agreement with the FE model in Fig. 10 validates the proposed coupled FE/ES computation scheme for the current problem. Fig 11 compares

Predicting range-dependent underwater sound propagation from structural sources in shallow water using coupled finite element/equivalent source computations

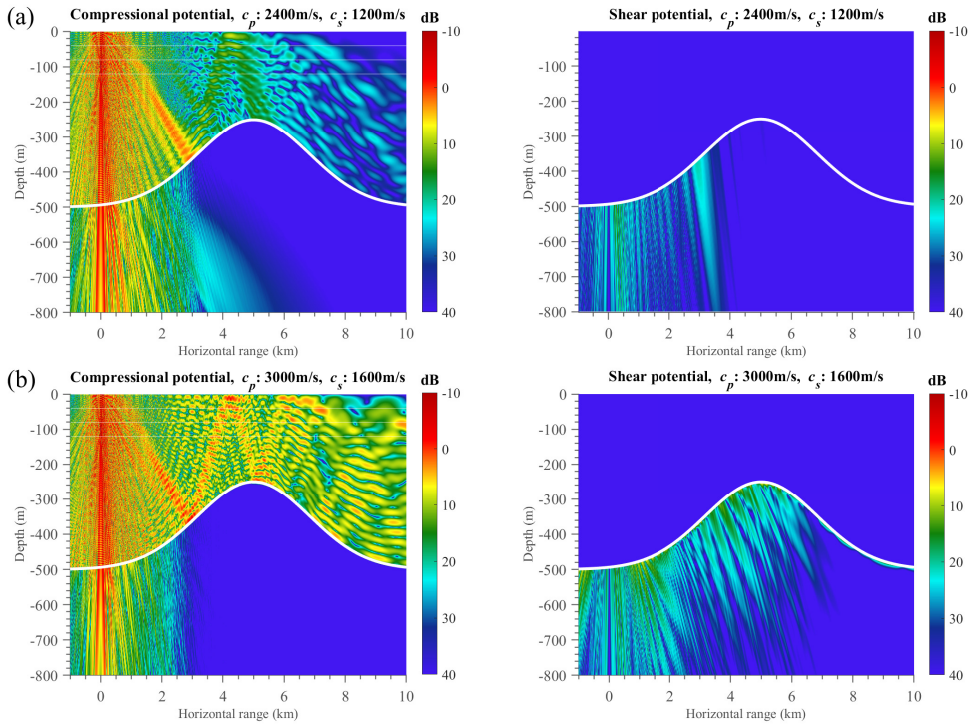


**Figure 8:** Sound propagation over the elastic Gaussian seamount in the whole computational domain at 150 Hz, with the upper and lower rows showing the results from the unconsolidated and consolidated seabed cases, respectively: (a). the compressional potential, and (b). the shear potential. The abscissa and ordinate of these graphs represent the horizontal range and the depth, respectively.

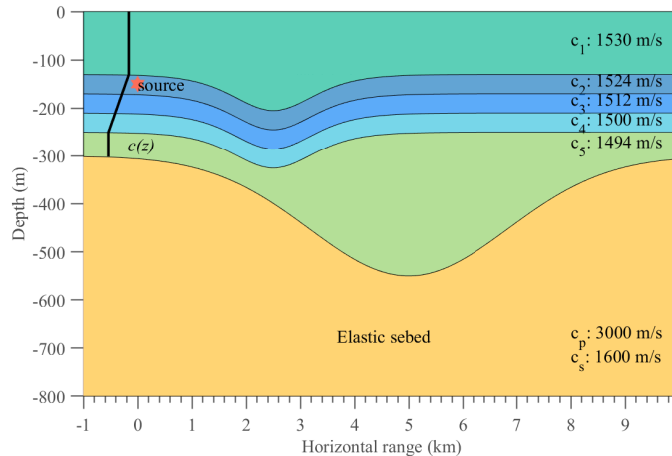


**Figure 9:** Schematic of the shallow water environment with an elastic Gaussian canyon in the presence of internal solitary waves. The abscissa and ordinate of the graph represent the horizontal range and the depth, respectively.

the waveguide field with and without the ISWs. The ISWs induce fluctuations in the sound speed structure of the water column, causing downward refractions that bend the acoustic rays toward the seabed and modal coupling. The former is reflected by the detailed field pattern (corresponding to the region from  $x = 1$  km to  $x = 3$  km and from  $z = -100$  m to  $z = -300$  m), and shifted to a steeper grazing angle to the canyon in the magnified plot of Fig. 11(a) compared with that of Fig. 11(b). The modal coupling transfers energy from high- to low-order modes, creating a triangular ‘shadow

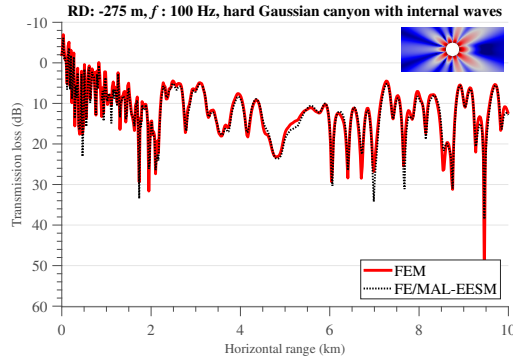


**Figure 10:** Transmission loss comparison with the FE model (red solid line) in the case of shallow water overlying a Gaussian canyon in the presence of internal solitary waves at 100 Hz, with the abscissa and ordinate representing the horizontal range and the transmission loss in dB, respectively. The receiver and source depths are 275 m and  $-150$  m, respectively.

zone' in Fig. 11(a) (corresponding to the region above  $z = -250$  m from  $x = 3$  km to  $x = 7$  km), over which the sound intensity is weaker than that in Fig. 11(b). Generally, as the sound propagates up-slope, mode cut-off occurs in mode sequences from high to low orders. Therefore, one can observe evidence of the energy transfer toward low-order modes by the high-order mode cut-off associated with the up-slope propagation around  $x = 9$  km in Fig. 11(b), which is absent in Fig. 11(a). By contrast, Fig. 11(a) exhibits more pronounced leakage of low-order modes near  $x = 10$  km than Fig. 11(b).

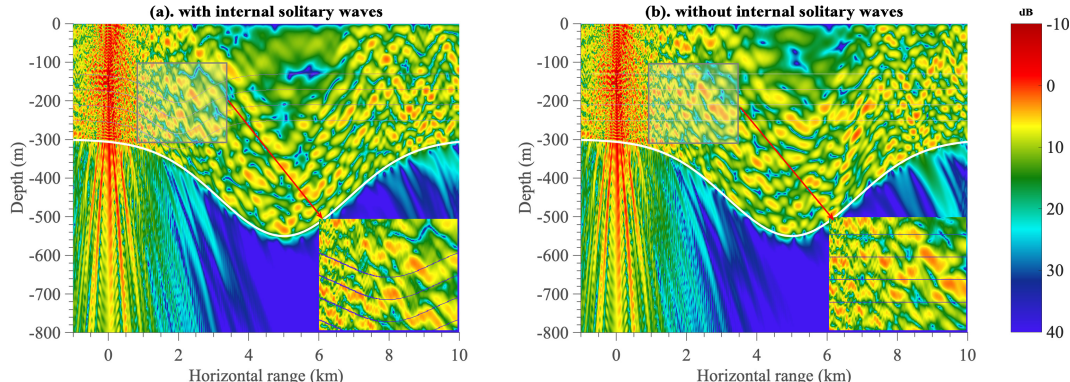


**Figure 11:** Sound propagation from the infinite cylindrical shell in shallow water overlying a Gaussian canyon with (a) and without (b) internal solitary waves. The shell is placed at  $z = -150$  m, driven by a point force loaded at the right-hand-side wall ( $0^\circ$ ) at 100 Hz. The magnified plots display the detailed field in the region extending from  $z = -100$  m to  $z = -300$  m and from  $x = 1$  km to  $x = 3$  km. The abscissa and ordinate of these graphs represent the horizontal range and the depth, respectively.

### Validity of ECDFM for calculating USP from a structural source in shallow water overlying a low-shear-speed seabed

Next, we perform parametric sweeps to test the validity of the ECDFM for calculating the USP from a structural source in shallow water overlying a low-shear-speed seabed. We consider two classical elastic seabed materials: sand and limestone. Jensen et al. (2011) The seabed parameters are given in Table 1, labeled as Seabed 3 and Seabed 4. The scenario considered here is a range-independent waveguide field excited by the same vibrating shell used in the previous simulations. The water depth is 300 m, and the shell is placed at a source depth of 150 m. We define the relative error  $E$  of the waveguide fields with the ECDFM approximation over the propagation range as:

$$E = \sqrt{\frac{\sum_{m=1}^M |p_{ECDF} - p_{ELA}|^2}{\sum_{m=1}^M |p_{ELA}|^2}}, \quad (32)$$

where  $p_{ELA}$  and  $p_{ECDF}$  are the sound pressures calculated with the elastic seabed model and with the ECDFM, respectively, and  $M$  is the number of sound pressure samplings. The sound pressure samplings are taken over the horizontal range from 0–10 km at a receiver depth of 150 m, with  $M = 1024$ . The parametric sweeps are performed for  $\theta_s$  against  $E$ , where  $\theta_s$  is defined as the angle between the direction of the dominant structural acoustic radiation and the seabed (see the upper column of Fig. 13 as an example of  $\theta_s = 0^\circ$ ). The left column of Fig. 12 gives the corresponding results in both the sand and limestone cases, from which the angular dependency of  $E$  can be observed. Overall, an increase in  $E$  is associated with increasing  $\theta_s$ , which coincides with the low-grazing angle approximation made in the ECDFM. To illustrate this further, the right column of Fig. 12 displays the plane wave reflection coefficients of the elastic seabed and the equivalent fluid seabed. The limestone case produces a larger  $E$  than the sand case because the fluid behavior does not adequately approximate the consolidated seabed's reflectivity. Interestingly, both cases exhibit a pronounced maximum in  $E$  at  $\theta_s = 45^\circ$ , meaning that the maximum may be related to the source directionality rather than the seabed type. To prove this further, Fig. 13(d) shows  $E$  as a function of  $\theta_s$  in the limestone case at 50 Hz and 150 Hz. Figs 13(a)–13(c) demonstrate the different directionalities of the shell vibrating at different frequencies with  $\theta_s = 0^\circ$ . One can observe that  $\theta_s$  corresponding to the maximum in  $E$  changes with the frequency, and the maximum vanishes in the 50 Hz case.

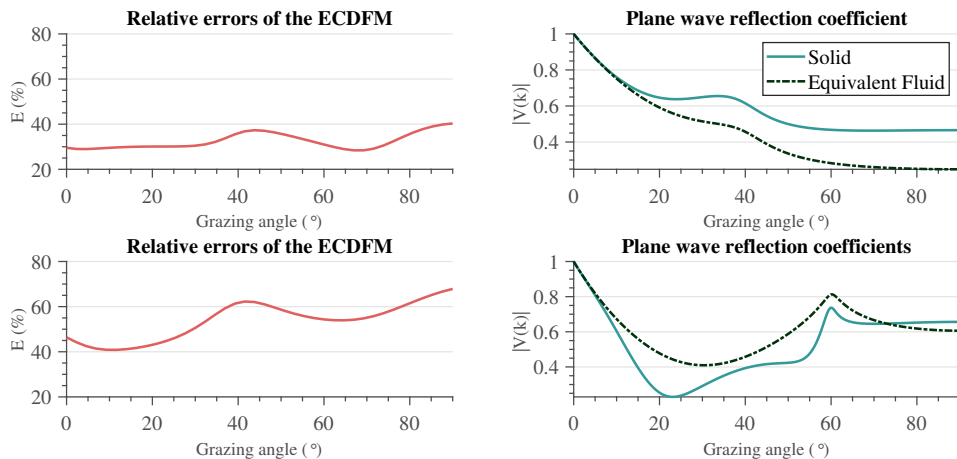


**Figure 12:** The relative error  $E$  of waveguide fields with the ECDFM approximation over the propagation range (left column) and the plane wave reflection coefficient of the elastic seabed and the equivalent fluid seabed (right column). The upper and lower rows give the relevant results in the sand and limestone cases, respectively. The abscissa of all these plots represents the grazing angle, and the ordinates of the plots in the left and right columns are the relative error and the reflection coefficient amplitude, respectively.

As the frequency increases, the source directionality becomes intense, with a main lobe carrying the dominant radiation energy and several nearby side lobes. The side lobes also carry considerable radiation energies [see Figs. 13(a)–13(c)]. As  $\theta_s$  increases, the energy of the side lobes gradually leaks into the seabed at the supercritical incidence. Moreover, the remaining energy carried by the main lobe propagates in the waveguide at a large subcritical grazing angle, for which the ECDFM is invalid. Therefore, the maximum in  $E$  may be associated with the main lobe propagating at large subcritical grazing angles. However, once  $\theta_s$  exceeds the seabed critical angle  $\theta_c$  sufficiently, both the main and side lobes are supercritically incident, so transmission is the dominant loss mechanism. This may explain the decrease in  $E$  with increasing  $\theta_s$  above  $45^\circ$ . Although the maximum in  $E$  changes for different source directionalities,  $E$  increases overall as  $\theta_s$  increases. This analysis suggests that the ECDFM is valid for calculating the USP from a structural source in shallow water overlying a low-shear-speed seabed when the source beam carrying the dominant radiation energy propagates at low grazing angles ( $\theta_s < \theta_c$ ). Note that this conclusion is

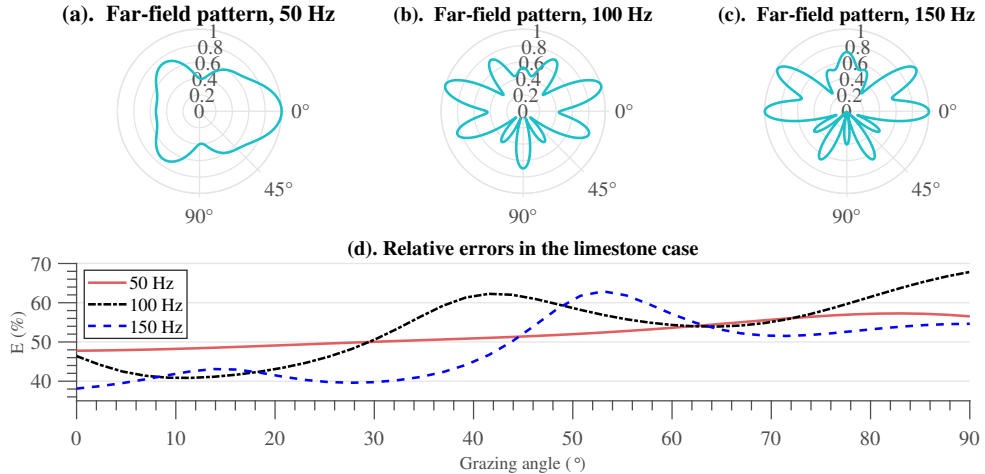


**Figure 13:** Directionalities of the shell vibrating at (a). 50 Hz, (b). 100 Hz, and (c). 150 Hz with  $\theta_s = 0$ , and (d). The relative error  $E$  of waveguide fields with the ECDFM approximation over the propagation range at these frequencies. The abscissa and ordinate of (d) are the grazing angle and the relative error.

based on the range-independent assumption. When a range-dependent seabed is considered, modal coupling, mainly determined by topographies and seafloor compressional-wave speeds rather than seafloor elasticity (compressional-to-shear conversion and shear-wave intromission), is likely to be the dominant loss mechanism. Therefore, the above conclusion is valid for most range-dependent circumstances.

### 3.2. 3D range-dependent USP from a structural source

#### 3.2.1. 3D coupled FE/ES analyses for vibroacoustics

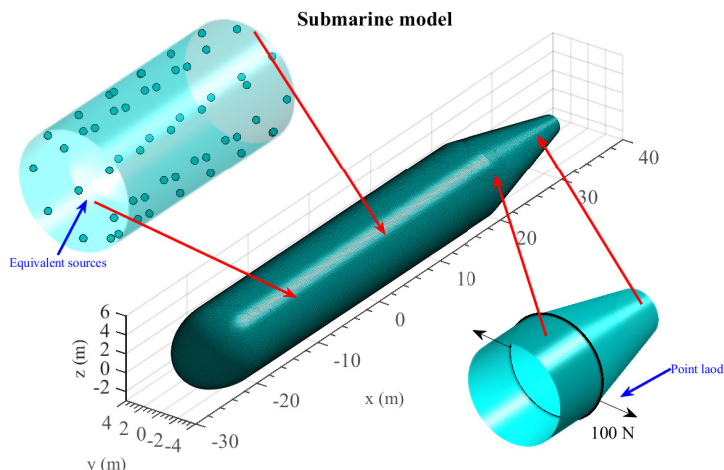


**Figure 14:** Schematic of the shell model considered in the FE model. The upper and lower magnified plots illustrate the ES distribution in the 3D case and the details of the point force loaded at the shell's wall, respectively.

This section presents simulations of the 3D range-dependent USP from a structural source in a complex shallow-water environment. As shown in Fig. 14, the 3D structural source is selected as a cylindrical shell with a semi-ellipsoid cap on one end and a cone tail on the other. The shell thickness is 0.08 m. The cylinder is 40 m in length and has a radius of 4 m. The equatorial and polar radii of the semi-ellipsoid are 4 m and 6 m, respectively. The cone has a height of 14 m with top and bottom radii of 1 m and 4 m, respectively. The shell vibration response is calculated using the solid mechanic module in COMSOL Multiphysics, and this response is used to couple the ES computation for

reproducing the structural-acoustic radiation. The shell's center is placed at the origin. The density, Young's modulus, and Poisson's ratio of the structural steel are the same as for the 2D case. A pair of normal point forces of 100 N acting in opposite directions (see the lower magnified figure in Fig. 14), loaded on the inner shell wall at (16 m, 4 m, 0 m) and (16 m, -4 m, 0 m), drives the shell to vibrate. The meshing scheme uses tetrahedrons to discretize the computation domain, with a maximum element size of 1/120 acoustic wavelengths.

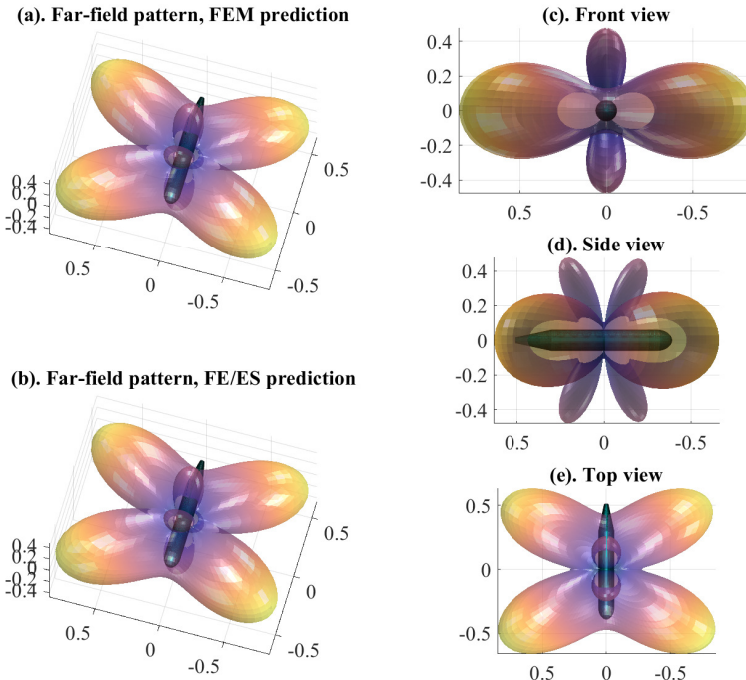


**Figure 15:** Far-field pattern of the point-force-driven shell vibrating at 25 Hz. The radial distance represents the magnitude of the normalized directionality.

After the coupled vibroacoustic FE/ES analyses, the incident field required by the 3D waveguide-field ES computation is produced by replacing the structural-acoustic radiation with the fields generated by a set of ESs within the shell. For this purpose, 500 ESs are uniformly distributed on a surface conformal to the shell with a scaling factor of 0.8 (see the upper magnified figure in Fig. 14). The ESs are located at the centers of boundary surface elements dividing the conformal surface. Fig 15 shows the far-field pattern of the shell vibrating at 25 Hz. To model the 3D FE far-field radiation, the tetrahedron mesh with a maximum element size of 1/6 acoustic wavelength is used to discretize a spherical computation domain with a radius of 60 m. The spherical computation domain is truncated by PMLs composed of 40 layers of swept meshes. Again, the predictions from the coupled FE/ES analyses are in excellent agreement with the FE results, confirming that the ES configuration and amplitudes can be used to evaluate the incident-field quantities required by a 3D ESM-based USP model. Note that the vertical directionality of the vibrating shell exhibits two pairs of sharp lobes at large grazing angles, the energy of which is likely to be attenuated by the supercritical incidence. Additionally, the grazing angle of the vertical main lobe is very shallow. This indicates that the ECDFM is valid for calculating the corresponding 3D USP from the current shell model vibrating at 25 Hz in shallow water over an unconsolidated seabed. This reduces the corresponding computational complexity, as we need only to use a 3D fluid USP model with the ECDFM.

### 3.2.2. 3D waveguide-field ES computation

#### Double seamount case

Based on the above analysis, the ECDFM can mimic the unconsolidated seabed, so the corresponding 3D range-dependent USP from the vibrating shell can be calculated with reduced computational complexity using a 3D fluid

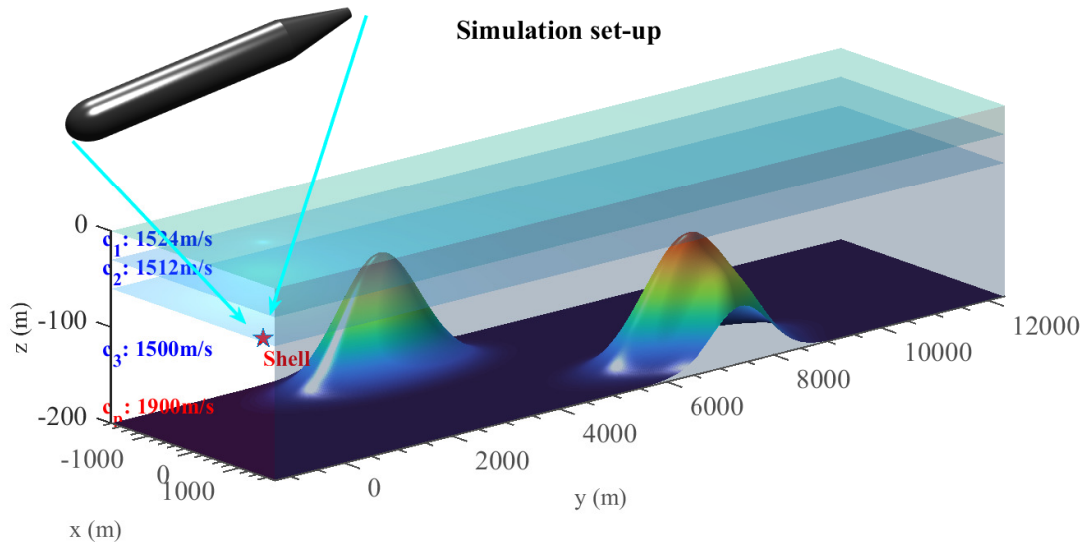


**Figure 16:** Simulation set-up for the coupled FE/ES computation for USP from the vibrating shell in a three-layer shallow water column overlying double unconsolidated seamounts.

USP model with the ECDFM. In this case, the PFFT-ESM is employed to calculate the 3D range-dependent USP from the vibrating shell over double unconsolidated seamounts. Seabed 3 (see Table 1) is used, as modeled by the ECDFM as an equivalent fluid seabed with a complex density (see the last column of Table 1). The discretization scheme of PFFT-ESM follows the rule of a maximum element size of six acoustic wavelengths in the  $x$ -,  $y$ -, and  $z$ -directions. As shown in Fig. 16, the 3D range-dependent shallow water environment treated in this simulation is a three-layer water column overlying the double-seamount topography. The seamounts are given by  $z_b(x, y) = h_0 + 70e^{-(x-x_0)^2/(2a_0^2)-(y-y_0)^2/(2b_0^2)} + 120e^{-(x-x_1)^2/(2a_1^2)-(y-y_1)^2/(2b_1^2)}$ , where  $h_0 = -200$  m,  $a_0 = a_1 = 300$ ,  $b_0 = 525$ , and  $b_1 = 750$ . For the near seamount,  $x_0 = 1600$  m,  $y_0 = 7400$  m,  $x_1 = 1000$  m, and  $y_1 = 7000$  m; for the distant seamount,  $x_0 = -1600$  m,  $y_0 = 3400$  m,  $x_1 = -1000$  m, and  $y_1 = 3000$  m. The sound speeds in the top two water layers decrease linearly from 1530 m/s to 1515 m/s with water depth, while the bottom water layer has a constant velocity of 1500 m/s, representing a classical summer profile. The shell is initially placed at a source depth of  $-100$  m, with the semi-ellipsoid cap toward the negative  $x$ -axis (corresponding to a source orientation of  $\theta = 0^\circ$ ). The computational domain spans  $6 \text{ km} \times 11 \text{ km} \times 225 \text{ m}$ .

Fig 17(a) shows the 3D range-dependent USP produced by the shell vibrating at 25 Hz in different horizontal and vertical planes. The ‘butterfly’ radiation pattern, featuring horizontal source directionality, can be observed at short ranges in the  $z = -150$  m plane. For  $\theta = 0^\circ$ , the butterfly-like radiation results in horizontal defocusing along the  $y$ -direction, which is intensified by the seamount scattering. This can be seen in the  $y = 3$  km and  $z = 0$  m planes. Two slices at  $x = 1$  km and  $x = -1$  km show apparent modal cut-off behaviors associated with up-slope propagation over the seamount. Figs 17(b) and 17(c) display the results with source orientations of  $\theta = 40^\circ$  and  $\theta = 90^\circ$  produced by rotating the source horizontally. The different source orientations share very similar interference patterns in the  $y$ - $z$  planes, which is caused by the near-omnidirectionality of the vibrating shell in this plane. However, when high-order vibration modes are excited at higher frequencies, discrepancies are expected to emerge in the vertical plane with different source orientations. With most radiation scattered by both the near and distant seamounts, the  $\theta = 40^\circ$  case exhibits horizontal focusing along the  $y$ -axis. Note that the scattering from the near seamount interferes with that from the distant seamount at long ranges, as can be seen in the slices at  $z = 0$  m in Fig. 17(b). The  $\theta = 90^\circ$  case is similar to  $\theta = 0^\circ$ , with horizontal defocusing as a result of the butterfly-like radiation and horizontal scattering by seamounts.

To further display the differences in the horizontal sound fields with different source orientations, Fig. 18 shows the depth-averaged TL with source orientations of  $\theta = 0^\circ$ ,  $\theta = 40^\circ$ , and  $\theta = 90^\circ$ . The depth-averaging is performed

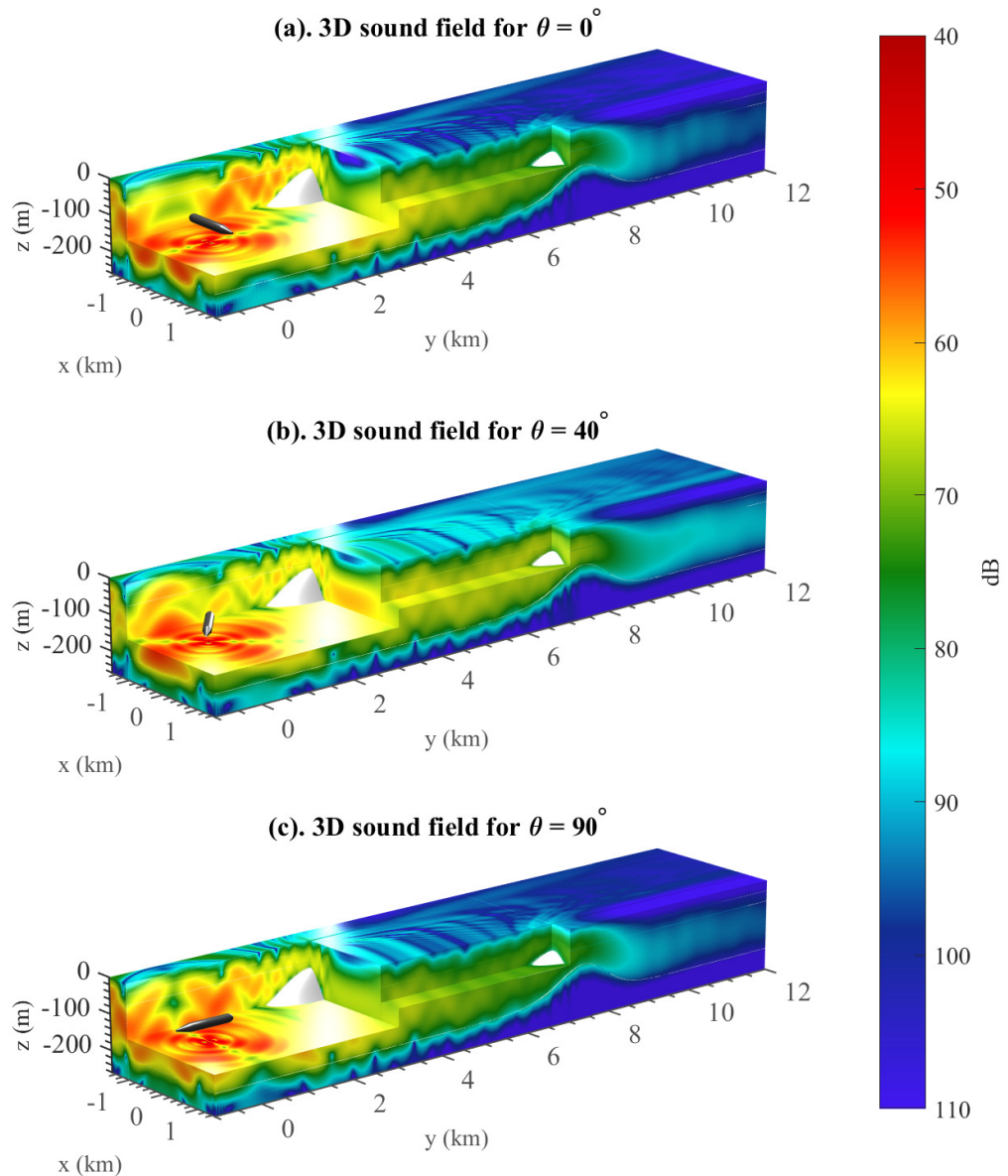


**Figure 17:** 3D range-dependent USP from the shell vibrating at 25 Hz, with source orientations of (a).  $\theta = 0^\circ$ , (b).  $\theta = 40^\circ$ , and (c).  $\theta = 90^\circ$ . The shell (displayed in black) is located at (0 km, 0 km, -100 m). The results are given by 3D TL contours, with the  $x > -1$  km region sliced at  $y = 3$  km and at  $z = -150$  m and then the  $x > 1$  km region sliced at  $y = 7$  km and at  $z = -100$  m.

at depth increments of 10 m. Despite the horizontal scattering, defocusing, and focusing effects observed from the 3D sound field analysis, the depth-averaged TL for  $\theta = 0^\circ$  shows the effects of horizontal refraction by the distant seamount at  $y = 7$  km, which bends the right-half radiation beam towards the  $x$ -axis. The  $\theta = 45^\circ$  case exhibits slight horizontal diffraction into shadow zones behind the distant seamount. Due to the butterfly-like radiation, only

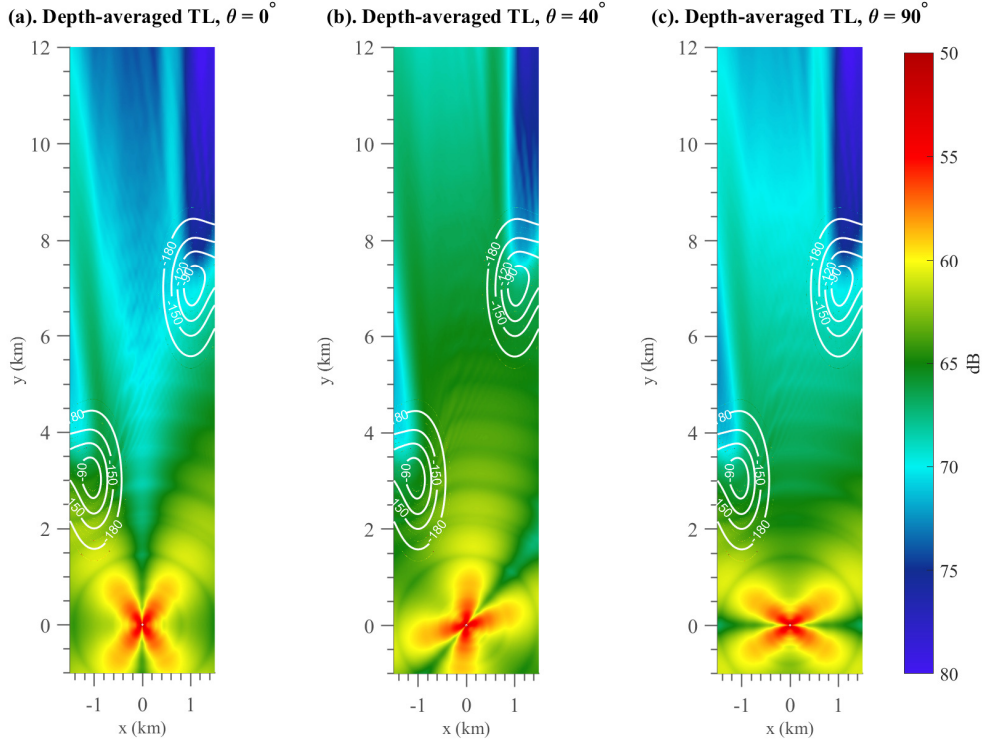


**Figure 18:** Depth-average TL with source orientations of (a).  $\theta = 0^\circ$ , (b).  $\theta = 40^\circ$ , and (c).  $\theta = 90^\circ$ . The abscissa and ordinate of these plots are the transverse and horizontal ranges, respectively.

the left-half radiation beam is scattered by the near seamount in the  $\theta = 90^\circ$  case. The above results demonstrate that the proposed 3D coupled FE/ES computation can account for the 3D propagation effects associated with a structural source, including horizontal scattering, refraction, and diffraction.

Although an N-2D computation can be implemented using the proposed 2D computation scheme, which is beneficial for achieving high numerical efficiency, there are limitations to such N-2D simulations. Since N-2D computation restricts the acoustic energy within a bearing plane and ignores the horizontal mode coupling across different bearing planes, it fails to consider horizontal refractions, scattering, and diffraction. By contrast, the proposed fully 3D computation scheme can accurately handle all these 3D propagation effects, which is very important when realistic underwater topographies are considered, such as seamount, underwater canyon, wedge, etc.

### 3.3. Discussion on numerical efficiency

This section discusses the numerical efficiency of the proposed coupled FE/ES computation scheme by comparison with a direct FE computation. The simulations described in this article were implemented using MATLAB (Matlab, Natick, MA) on a computer with an Intel Core i9-10900K CPU and 96 GB RAM (Intel, Santa Clara, CA). The proposed scheme is of a two-fold procedure, including a coupled vibroacoustic FE/ES analysis and a waveguide-field ES computation for propagating the structural-acoustic radiation in shallow water. The numerical cost of the coupled vibroacoustic FE/ES analyses is at  $O(N_{DOF_f}^{2-3}) + O(N_{eq_f}^{2-3})$ , where  $N_{DOF_f}$  and  $N_{eq_f}$  represent the degrees of freedom (DOF) of the FE computation and the ES number for replacing the structural-acoustic radiation, respectively. Similarly, the numerical cost of the waveguide-field ES computation depends on the ES number for replacing the waveguide field ( $N_{eq_w}$ ). Therefore, the total numerical cost of the proposed scheme is at  $O(N_{DOF_f}^{2-3}) + O(N_{eq_f}^{2-3}) + O(N_{eq_w}^{2-3})$ . On the other hand, the direct FE computation couples both the radiation and propagation processes. Given the DOF in direct FE computation ( $N_{DOF_d}$ ), the corresponding numerical cost is at  $O(N_{DOF_d}^{2-3})$ . It is worth mentioning that the ESM-based USP model reduces the problem dimensions compared with the direct FE computation by only discretizing the waveguide's boundaries, and  $N_{DOF_f}$  is significantly smaller than  $N_{DOF_d}$  because the computational domain in the

**Table 2**

Analysis of the numerical cost and the average computation time required by the proposed coupled FE/ES computation scheme and the full FEM in the 2D computation case at 150 Hz.

	Coupled FE/ES			Direct FE
	FE	ES	Waveguide-field ES	FE
$N_{un}$	$2.29 \times 10^6$	$3.6 \times 10^2$	$6.627 \times 10^4$	$2.937 \times 10^7$
$O$	$O(10^{18})$	$O(10^7)$	$O(10^{14})$	$O(10^{22})$
$t$	1 mins 10 s	0.23 s	18 mins 20 s	40 mins 10 s

coupled FE/ES analysis is only at the size of the structure while that in the direct FE computation is of thousands of wavelengths. Therefore, it is anticipated that  $O(N_{DOF_f}^{2-3}) + O(N_{eq_f}^{2-3}) + O(N_{eq_w}^{2-3})$  would be significantly lower than  $O(N_{DOF_d}^{2-3})$ , especially for 3D scenarios.

Table. (2) then analyses the numerical cost and the average computation time required by the proposed coupled FE/ES computation scheme and the direct FE computation in the 2D case at 150 Hz (Gaussian seamount case). As expected,  $N_{DOF_d}$  is at four order of number higher than  $N_{DOF_f}$ ,  $N_{eq_f}$ , and  $N_{eq_w}$ . Therefore, the direct FE computation is more numerically expensive than the proposed scheme, taking almost two times the computation time.

As for the numerical efficiency of the proposed scheme for the 3D simulation, the most numerically expensive step is PFFT-ESM. Further details about the discussion on the numerical efficiency of PFFT-ESM are presented by He *et al.* He et al. (2021a). The conclusion is that a direct FE computation remains computationally challenging for the present problem to be run on a standard computer, while the proposed scheme incorporating PFFT-ESM costs about  $O(N_{eq_w} \log N_{eq_w})$  operations, enabling the present fully-3D problem to be solved. The iterative tolerance was set to be  $5 \times 10^{-3}$ , and the PFFT-ESM converged after 431 iterations, which took about 5 hours.

#### 4. Conclusions

This article has presented a coupled FE/ES computation scheme for predicting the range-dependent USP from a structural source in complex shallow water. The proposed scheme includes a coupled vibroacoustic FE/ES analysis for replacing the structural-acoustic radiation with a set of ESs within the source and a waveguide-field ES computation for propagating the structural-acoustic radiation in shallow water.

Simulations have demonstrated the validity and capability of the proposed scheme for coupling structural acoustic radiation and complex ocean environments. The 2D simulations validated the proposed scheme, confirming it provides benchmark-quality solutions and high numerical efficiency. Parameter sweeps were performed to explore the validity of the ECDFM for calculating the waveguide field excited by a structural source over a low-shear-speed elastic seabed. The analysis suggests that acceptable results can be obtained by a fluid USP model with the ECDFM when the main lobe of the radiation is subcritically incident. Based on these results, the proposed scheme was extended to 3D range-dependent USP from a vibrating shell over a double unconsolidated seamount. The modal cut-off associated with the up-slope propagation and the horizontal scattering by the seamount indicate that the presented 3D results are reasonable. This article has demonstrated the potential of the proposed coupled FE/ES computation scheme to be a useful tool in the preliminary design and optimization of sonar performance.

The original contributions of this work are:

- A coupled FE/ES computation scheme has been proposed to model the range-dependent acoustic propagation from a vibrating structural source in both 2D and 3D, with the capability for coupling structural-acoustic radiations with horizontally inhomogeneous waveguides. This feature makes the proposed scheme significant, as most existing hybrid algorithms can only handle horizontally homogeneous shallow water acoustic environments.
- A novel multilayer acoustic–elastic ESM is developed to extend the ESM-based acoustic propagation model, allowing sound speed inhomogeneities and range-dependent elastic seabeds to be accommodated.
- The validity of ECDFM has been analyzed for calculating the waveguide field excited by a structural source, suggesting that a fluid sound propagation model can incorporate with the ECDFM for approximating the reflectivity of unconsolidated seafloor once the main lobe of the radiation is subcritically incident.

## 5. Acknowledgments

This work was supported by the National Natural Science Foundation of China (Grand No. 52101387), State Key Laboratory of Ocean Engineering (Shanghai Jiao Tong University) (Grant No. GKZD010084), and Fund of Key Laboratory of National Defense Science and Technology (Grant No. 2021-JCJQ-LB-066-09).

## References

- Abawi, A.T., Porter, M.B., 2007. Propagation in an elastic wedge using the virtual source technique. *The Journal of the Acoustical Society of America* 121, 1374–1382.
- Badiey, M., Katsnelson, B.G., Lynch, J.F., Pereselkov, S., Siegmann, W.L., 2005. Measurement and modeling of three-dimensional sound intensity variations due to shallow-water internal waves. *The Journal of the Acoustical Society of America* 117, 613–625.
- Bottero, A., Cristini, P., Komatitsch, D., Asch, M., 2016. An axisymmetric time-domain spectral-element method for full-wave simulations: Application to ocean acoustics. *The Journal of the Acoustical Society of America* 140, 3520–3530.
- Bottero, A., Cristini, P., Komatitsch, D., Brissaud, Q., 2018. Broadband transmission losses and time dispersion maps from time-domain numerical simulations in ocean acoustics. *The Journal of the Acoustical Society of America* 144, EL222–EL228.
- CA Oliveira, T., Lin, Y.T., 2019. Three-dimensional global scale underwater sound modeling: The T-phase wave propagation of a Southern Mid-Atlantic Ridge earthquake. *The Journal of the Acoustical Society of America* 146, 2124–2135.
- Collins, M.D., Evans, R.B., 1992. A two-way parabolic equation for acoustic backscattering in the ocean. *The Journal of the Acoustical Society of America* 91, 1357–1368.
- Cristini, P., Komatitsch, D., 2012. Some illustrative examples of the use of a spectral-element method in ocean acoustics. *The Journal of the Acoustical Society of America* 131, EL229–EL235.
- Decourcy, B.J., Duda, T.F., 2020. A coupled mode model for omnidirectional three-dimensional underwater sound propagation. *The Journal of the Acoustical Society of America* 148, 51–62.
- Fahline, J.B., 2021. Improved accuracy for radiation damping in coupled finite element/equivalent source computations. *The Journal of the Acoustical Society of America* 150, 2375–2387.
- Godinho, L., Tadeu, A., Branco, F., 2001. 3D acoustic scattering from an irregular fluid waveguide via the BEM. *Engineering Analysis with Boundary Elements* 25, 443–453.
- He, T., Humphrey, V.F., Mo, S., Fang, E., 2020. Three-dimensional sound scattering from transversely symmetric surface waves in deep and shallow water using the equivalent source method. *The Journal of the Acoustical Society of America* 148, 73–84.
- He, T., Mo, S., Fang, E., Wang, M., Zhang, R., 2021a. Modeling three-dimensional underwater acoustic propagation over multi-layered fluid seabeds using the equivalent source method. *The Journal of the Acoustical Society of America* 150, 2854–2864.
- He, T., Mo, S., Guo, W., Fang, E., 2021b. Modeling propagation in shallow water with the range-dependent sea surfaces and fluid seabeds using the equivalent source method. *The Journal of the Acoustical Society of America* 149, 997–1011.
- Huang, H., Zou, M.S., Jiang, L.W., 2019a. Study of integrated calculation method of fluid-structure coupling vibrations, acoustic radiation, and propagation for axisymmetric structures in ocean acoustic environment. *Engineering Analysis with Boundary Elements* 106, 334–348.
- Huang, H., Zou, M.S., Jiang, L.W., 2019b. Study on the integrated calculation method of fluid-structure interaction vibration, acoustic radiation, and propagation from an elastic spherical shell in ocean acoustic environments. *Ocean Engineering*, 29–39.
- Isakson, M.J., Chotiros, N.P., 2011. Finite element modeling of reverberation and transmission loss in shallow water waveguides with rough boundaries. *The Journal of the Acoustical Society of America* 129, 1273–1279.
- Isakson, M.J., Goldsberry, B., Chotiros, N.P., 2014. A three-dimensional, longitudinally-invariant finite element model for acoustic propagation in shallow water waveguides. *The Journal of the Acoustical Society of America* 136, EL206–EL211.
- Jensen, F.B., Kuperman, W.A., Porter, M.B., Schmidt, H., 2011. Computational ocean acoustics. Springer Science & Business Media.
- Jia-xi, D., Lin, Z., Xue-hai, S., Wen-jing, C., Liang-long, D., 2021. An equivalent source CVIS method and its application in predicting structural vibration and acoustic radiation in ocean acoustic channe. *Ocean Engineering* 222, 108570.
- Jiang, L.W., Zou, M.S., Liu, S.X., Huang, H., 2020. Calculation method of acoustic radiation for floating bodies in shallow sea considering complex ocean acoustic environments. *Journal of Sound and Vibration* 476, 115330.
- Keltie, R., 1986. The effect of hydrostatic pressure fields on the structural and acoustic response of cylindrical shells. *The Journal of the Acoustical Society of America* 79, 595–603.
- Koopmann, G.H., Song, L., Fahline, J.B., 1989. A method for computing acoustic fields based on the principle of wave superposition. *The Journal of the Acoustical Society of America* 86, 2433–2438.
- Li, C., Campbell, B.K., Liu, Y., Yue, D.K., 2019. A fast multi-layer boundary element method for direct numerical simulation of sound propagation in shallow water environments. *Journal of Computational Physics* 392, 694–712.
- Liu, W., Zhang, L., Wang, W., Wang, Y., Ma, S., Cheng, X., Xiao, W., 2021. A three-dimensional finite difference model for ocean acoustic propagation and benchmarking for topographic effects. *The Journal of the Acoustical Society of America* 150, 1140–1156.
- Oliveira, T.C., Lin, Y.T., Kushida, N., Jesus, S.M., Nielsen, P., 2021. T-wave propagation from the Pacific to the Atlantic: The 2020 MW 7.4 kermadec trench earthquake case. *JASA Express Letters* 1, 126001.
- Pan, C., Sun, X., Zhang, Y., 2020. Vibro-acoustic analysis of submerged ring-stiffened cylindrical shells based on a symplectic wave-based method. *Thin-Walled Structures* 150, 106698.
- Peng, Y., Tsouvalas, A., Stampoultzoglou, T., Metrikine, A., 2021. A fast computational model for near- and far-field noise prediction due to offshore pile driving. *The Journal of the Acoustical Society of America* 149, 1772–1790.
- Pereira, A., Tadeu, A., Godinho, L., Santiago, J., 2010. 2.5 D BEM modeling of underwater sound scattering in the presence of a slippage interface separating two flat layered regions. *Wave Motion* 47, 676–692.

## Predicting range-dependent underwater sound propagation from structural sources in shallow water using coupled finite element/equivalent source computations

- Petnikov, V.G., Grigorev, V.A., Lunkov, A.A., Sidorov, D.D., 2022. Modeling underwater sound propagation in an arctic shelf region with an inhomogeneous bottom. *The Journal of the Acoustical Society of America* 151, 2297–2309.
- Petris, G., Cianferra, M., Armenio, V., 2022. A numerical method for the solution of the three-dimensional acoustic wave equation in a marine environment considering complex sources. *Ocean Engineering* 256, 111459.
- Porter, M.B., 2019. Beam tracing for two-and three-dimensional problems in ocean acoustics. *The Journal of the Acoustical Society of America* 146, 2016–2029.
- Sturm, F., 2016. Leading-order cross term correction of three-dimensional parabolic equation models. *The Journal of the Acoustical Society of America* 139, 263–270.
- Tu, H., Wang, Y., Yang, C., Wang, X., Ma, S., Xiao, W., Liu, W., 2022. A novel algorithm to solve for an underwater line source sound field based on coupled modes and a spectral method. *Journal of Computational Physics* 468, 111478.
- Wu, S., Xiang, Y., Qin, T., 2022. A novel hybrid superposition method for predicting ship seismic wave in shallow sea. *Ocean Engineering* 259, 111948.
- Zhang, Z., Tindle, C., 1995. Improved equivalent fluid approximations for a low shear speed ocean bottom. *The Journal of the Acoustical Society of America* 98, 3391–3396.
- Zou, M.S., Liu, S.X., Jiang, L.W., Huang, H., 2020. A mixed analytical-numerical method for the acoustic radiation of a spherical double shell in the ocean-acoustic environment. *Ocean Engineering* 199, 107040.